

Numerical Analysis of the Effect of Diffusion and Creep Flow on Cavity Growth

J. Oh¹, N. Katsube² and F.W. Brust³

Abstract: In this paper, intergranular cavity growth in regimes, where both surface diffusion and deformation enhanced grain boundary diffusion are important, is studied. In order to continuously simulate the cavity shape evolution and cavity growth rate, a fully-coupled numerical method is proposed. Based on the fully-coupled numerical method, a gradual cavity shape change is predicted and this leads to the adverse effect on the cavity growth rate. As the portion of the cavity volume growth due to jacking and viscoplastic deformation in the total cavity volume growth increases, spherical cavity evolves to V-shaped cavity. The obtained numerical results are physically more realistic compared to results in the previous works. The present numerical results suggest that the cavity shape evolution and cavity growth rate based on the assumed cavity shape, spherical or crack-like, simply cannot be used in this regime.

Keyword: cavity growth, diffusion, creep flow, intercrystalline fracture

1 Introduction and Literature Review

At high temperature, cavity initiation and cavity growth are important phenomena in understanding the failure mechanism, and in predicting the lifetime of various parts in service in the area of a power plant and aero space applications, among others. Such nucleation and growth phenomena are explained by a diffusion of atomic flux (from

cavity surface to grain boundary), creep flow, and grain boundary sliding. Because of the complexity of the physical phenomenon, in most of the previous works, one of the two extreme cases, fast grain boundary diffusion or fast surface diffusion, with or without the consideration of grain material creep flow, is assumed.

When grain boundary diffusivity is much faster than surface diffusivity (surface diffusion controlled process), the cavity shape will be similar to a crack because the atomic flow rate along the cavity surface is not fast enough to reduce the surface curvature at the cavity tip. On the other hand, when surface diffusivity is much faster than grain boundary diffusivity (grain boundary diffusion controlled process), the cavity shape will be a spherical cap shape.

The basic model for predicting a grain boundary diffusion dominant cavitation process was first proposed by Hull and Rimmer (1959) (see Fig. 1(a)). Speight and Harris (1967) and Weertman (1973) included proper boundary conditions in the Hull-Rimmer (1959) model. Their model predicts the cavity growth rate in the rigid surrounding material with the assumption of a grain boundary diffusion controlled process. Vitek (1978) calculated cavity growth rates taking into consideration the deformation of the surrounding elastic material. Raj (1975) considered the events occurring during the elastic transient time. However, in the above models, plastic material deformation of the grain material is neglected, and the surface diffusivity is assumed to be much faster than the grain boundary diffusivity.

Beere and Speight (1978) and Edward and Ashby (1979) attempted to model the combined effect of creep flow of the surrounding grain material and the grain boundary diffusion process on the cavity

¹ Samsung Electronics Co., San #16 Banwol-Ri, Taeaneup, Hwasung-City, Gyeonggi-Do, Korea, 445-701. joonyoung. Email: oh@samsung.com.

² Mechanical Engineering, Ohio State University, 650 Ackerman rd., Columbus, Ohio, 43202. Tel: 614-292-0971, E-mail: katsube.1@osu.edu.

³ Battelle Memorial Institute, 505 King Avenue, Columbus, Ohio 43201-2693. E-mail: Brust@battelle.org.

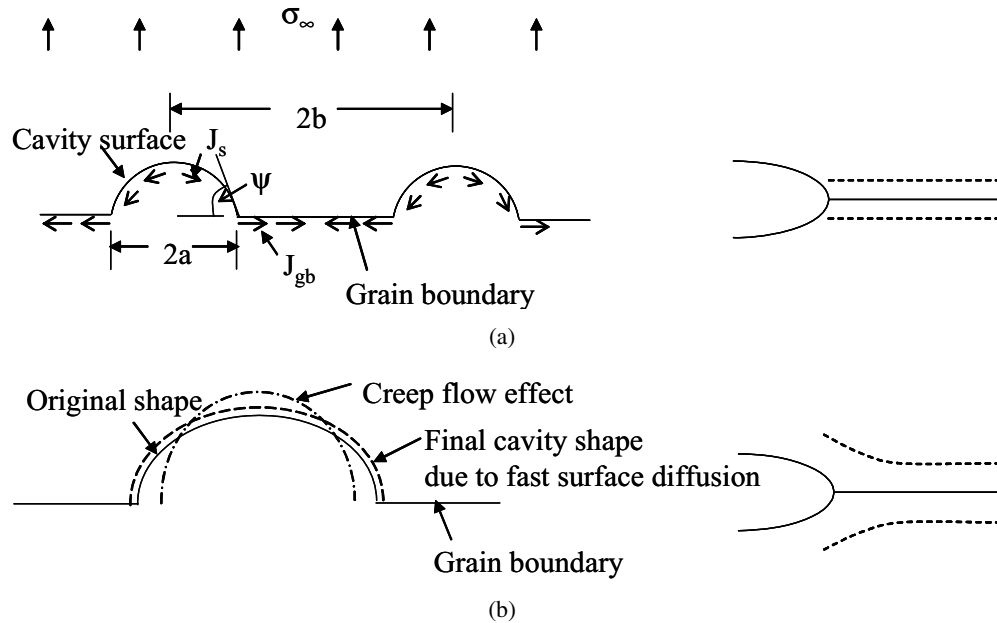


Figure 1: (a) Hull-Rimmer type diffusion flow along cavity surface and grain boundary. The grain boundary separate as rigid bodies. (b) The effect of creep flow on grain boundary diffusion. The deformation of the grain material causes local accommodation at the cavity tip.

growth. However, in these two models, it is assumed that elastic material surrounds the cavity. Needleman and Rice (1980) established a numerical approach based on the variational principle for creep flow and grain boundary diffusion coupled problems and obtained a finite element solution for the cavity growth rate. Figure 1(b) shows the effect of the creep flow on the grain boundary diffusion and the updated spherical cavity profile based on the assumption of the fast surface diffusion.

The assumption of the grain boundary controlled cavitation may not always be satisfied, and elongated rupture cavities are sometimes observed. Thus, Chuang and Rice (1973), Chuang et al. (1979), and Pharr and Nix (1979) analyzed the surface diffusion controlled process (no deformation or grain boundary diffusion included). Chuang et al. (1979) studied crack-like cavity volume growth by solving the Nernst-Einstein surface diffusion equation. Assuming an initial crack-like cavity shape, they obtained the steady state solution for cavity growth. Martinez and Nix (1982) extended the Finite Difference approach by Pharr and Nix (1979) to study cavity evolu-

tion from an initial spherical-shaped cavity to a crack-like cavity and verified their results against the experimental data by Goods and Nix (1978).

Since the development of the variational principle approach by Needleman and Rice (1980), further studies have been performed to analyze the combined phenomena of the grain boundary diffusion and the surface diffusion (Pan and Cocks (1993a, 1993b, 1995), Cocks and Pan (1993), Suo and Wang (1994), and Sun, Suo and Cocks (1996)). The main problems in coupling the surface and grain boundary diffusions are to satisfy three physical boundary conditions at the cavity tip, i.e., the continuity of the chemical potential, equilibrium dihedral angle, and matter conservation law. While they successfully overcome these problems, the diffusion element used by the above researchers can be used only for a rigid material.

Despite its apparent importance, a fully coupled continuous cavity growth analysis has never been attempted. The numerical studies of these combined effects on the cavity growth will provide a basic understanding of these synergies, and they will be useful in identifying the critical conditions where the combined effects become important.

In this work, the fully-coupled numerical method is proposed to study cavity shape evolution and cavity growth rate, where the surface and grain boundary diffusion and material viscoplastic deformation are considered. The proposed fully-coupled method continuously describes the cavity shape change and cavity growth in the regimes where both surface diffusion and deformation enhanced grain boundary diffusion are important. It is shown that the cavity growth rate based on the fully-coupled method is faster than that based on the combined cavity shape assumption in the cavity shape transition region. This is attributed to the gradual cavity shape change from the spherical to the crack-like.

In addition, it is shown that the spherical cavity evolves to the V-shaped cavity under conditions where both surface diffusion and deformation enhanced grain boundary diffusion are important. It is attributed to the jacking and cavity shape change due to viscoplastic deformation in the fully-coupled method. The cavity shape evolution from the spherical cavity to the V-shaped cavity, which was experimentally observed but has never been predicted, is numerically predicted in this work.

Recent work by Yuan and Zhang (2006) considered the effect of cavity nucleation as well as growth in incompressible transversely isotropic nonlinearly elastic materials. Both nucleation and the effects of non-isotropic material response are not considered here.

It is shown that the cavity shape change is directly connected to the life prediction of the structure. Therefore, the fully-coupled method which can monitor the continuous cavity shape change is crucial for accurately predicting the remaining life of the structure.

2 Methodology

The atomic flow rates are proportional to driving forces, which are chemical potential gradients of the atom. When tensile stress is applied on the grain boundary, atoms diffuse from the cavity surface to the grain boundary due to the chemical potential gradient. As atoms diffuse from the cav-

ity wall to the grain boundary, the grain boundary should accommodate the diffused atoms.

The chemical potential of the atom on the cavity surface ' μ_s ' and that on the grain boundary ' μ_{gb} ' respectively, are given by

$$\begin{aligned}\mu_s &= -\gamma_s(\kappa_1 + \kappa_2)\Omega \\ \mu_{gb} &= -\sigma_N\Omega\end{aligned}\quad (1)$$

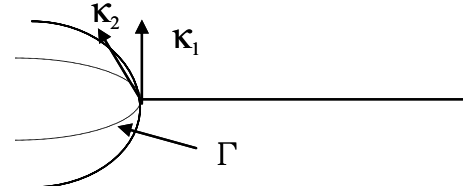


Figure 2: Principal curvatures at cavity tip, 1 in the plane perpendicular to the grain boundary and 2 in the plane of the grain boundary, are shown, where arrow shows the tangent direction of each curvature. Intersection of the grain boundary and the cavity surface is shown by Γ (Γ is in the plane of the grain boundary).

The atomic volume, surface tension at cavity surface, two principal curvatures of the cavity surface, and normal stress along the grain boundary are respectively represented by ' Ω ', ' γ_s ', ' κ_1 ', ' κ_2 ', and ' σ_N '. In Fig. 2, the definition of the two principal curvatures for the axis-symmetric cavity surface is shown. The driving force of the surface diffusion denoted by ' F_s ' and that of the grain boundary diffusion denoted by ' F_{gb} ', respectively, are

$$\begin{aligned}F_s &= -\frac{\partial\mu_s}{\partial S} \\ F_{gb} &= -\frac{\partial\mu_{gb}}{\partial r}\end{aligned}\quad (2)$$

where ' S ' is the curvilinear coordinate along the cavity surface and ' r ' is the radial coordinate from the center of the cavity. Assuming the linear kinetic law, the surface and grain boundary atomic flow rates, denoted by ' j_s ' and ' j_{gb} ', respectively, are given by Eq. (3).

$$\begin{aligned}j_s &= M_s F_s \\ j_{gb} &= M_{gb} F_{gb}\end{aligned}\quad (3)$$

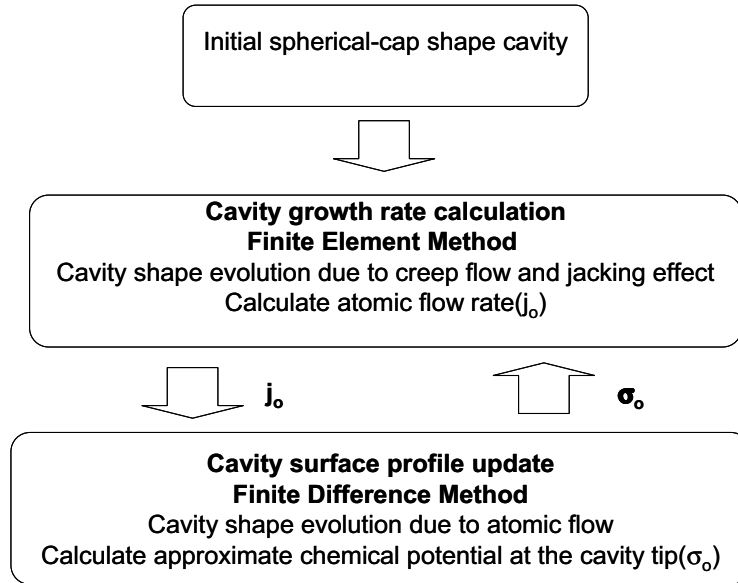


Figure 3: Illustration of numerical calculation structure for single cavity growth model. The unified numerical method, which combines finite element method and finite difference method, starts with the known spherical-cap shape cavity geometry. For the given time step, which is chosen to be sufficiently short, finite element method and finite difference method are employed to simulate cavity shape evolution.

where ' M_s ' and ' M_{gb} ' are given by

$$\begin{aligned} M_s &= \frac{D_s}{kT}, & D_s &= D_{so} \delta_s \exp\left(-\frac{Q_s}{RT}\right), \\ M_{gb} &= \frac{D_{gb}}{kT}, & D_{gb} &= D_{gbo} \delta_{gb} \exp\left(-\frac{Q_{gb}}{RT}\right). \end{aligned} \quad (4)$$

In the above equation, ' D_s ', ' D_{gb} ', ' k ', ' T ', ' $D_{so} \delta_s$ ', ' $D_{gbo} \delta_{gb}$ ', ' Q_s ', ' Q_{gb} ', and ' R ' respectively, are the surface diffusivity, grain boundary diffusivity, Boltzman constant, absolute temperature, surface diffusion coefficient, grain boundary diffusion coefficient, activation energy for surface diffusion, activation energy for grain boundary diffusion, and gas constant.

In this work, cavity growth rates and cavity shape evolution are calculated by combining finite element and finite difference methods for a given time step. First, an extended version of the FE method by Needleman and Rice (1980) is used to evaluate the cavity growth rate. This consists of the contribution due to the atomic flow rate from the cavity surface to the grain boundary and that due to the cavity shape change caused by deformation and the phenomena called "jacking". The "jacking" effect refers to the upward move-

ment of the grain boundary and the cavity surface perpendicular to the grain boundary due to the atomic diffusion from the cavity surface to the grain boundary.

Second, the open ended finite difference method by Pharr and Nix (1979) is used to update the cavity shape for a given atomic rate j_o ($j_o = j_{gb}$ at the cavity tip). After the cavity shape evolves for the current time step, the chemical potential of the atom at the cavity tip is calculated approximately from the value of principal curvatures of the node next to the cavity tip. At the next time step, the cavity tip stress (σ_o) is calculated from the cavity tip curvatures and will be used as an input for the FEM portion of the analysis. The same procedure is repeated until cavity coalescence occurs. In Fig. 3, the structure of this numerical procedure is shown.

In combining the FEM and FDM method, numerical determination of the cavity tip position is necessary. The following numerical procedure is developed for this purpose. After modeling the grain boundary diffusion and grain material deformation (Finite Element analysis), the original cavity tip node moves upward due to the "jacking" ef-

fect. However, before starting the cavity evolution simulation (Finite Difference analysis), this node needs to move back to somewhere on the grain boundary since the cavity tip node must always be on the original grain boundary. The new position is determined so that the local tension equilibrium condition shown in Fig. 4 is satisfied.

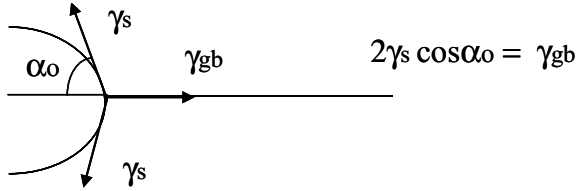


Figure 4: Equilibrium dihedral angle (α_o) satisfying the local tension equilibrium condition, where γ_s and γ_{gb} are cavity surface tension and grain boundary surface tension, respectively.

As shown in Fig. 4, the force equilibrium condition between the cavity surface tension (γ_s) and the grain boundary tension (γ_{gb}) determines the equilibrium angle α_o . The position of the cavity tip node is numerically determined to satisfy this equilibrium angle. In order to physically explain this nodal movement and the associated local cavity shape change, additional matter diffusion within the cavity surface needs to be introduced.

In Fig. 5, this additional matter diffusion accompanied by the “jacking” phenomena is explained. In Fig. 5(a), the movement of the cavity surface and the grain boundary after FEM analysis at time $t + \Delta t$ is shown. The cavity surface and the grain boundary move up due to the volume of the diffused atoms and new cavity surface is created. In order to maintain the equilibrium angle at the newly created cavity surface, local rearrangement of atoms (the additional matter flow δj_s) becomes necessary. In Fig. 5(b), the cavity surface satisfying the equilibrium angle is shown, where the additional matter flow δj_s is considered. This surface shape is used for the FDM analysis.

2.1 Finite Element Method

As the starting point, the finite element formulation by Needleman and Rice (1980) is imple-

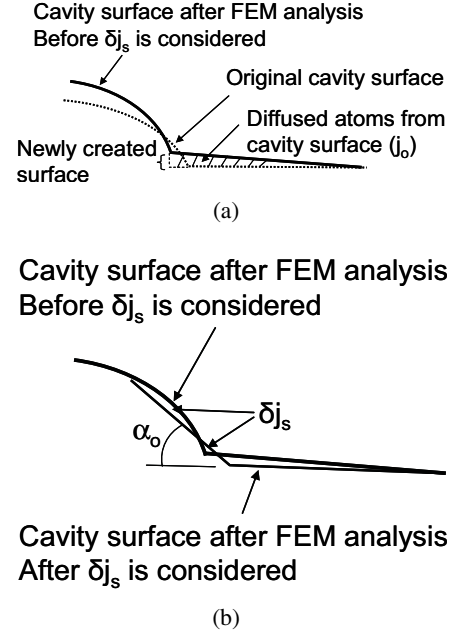


Figure 5: (a) The cavity surface and the grain boundary shape at time $t + \Delta t$ after FEM analysis is done. The additional flow δj_s is not considered. The grain boundary and the cavity surface at time t moves up due to the volume of the diffused atoms. The newly created cavity surface at the cavity tip is not at equilibrium angle. (b) The cavity surface and the grain boundary shape at time $t + \Delta t$ before starting FDM analysis. The additional flow δj_s is necessary to satisfy the equilibrium angle at the newly created surface.

mented to consider the effect of viscoplastic material deformation and grain boundary diffusion on cavity growth. With this approach, the diffusive flux along the cavity surface was not considered and the cavity shape could not be changed from the initial spherical cap shape. Following Needleman and Rice (1980), the functional, \bar{F}_{gb} , is given by,

$$\bar{F}_{gb} = \int_V \omega(\dot{\epsilon}_{kl})dV - \int_{S_T} T_i v_i dS + \int_{A_{gb}} \frac{j_\alpha j_\alpha}{2M_{gb}\Omega} dA + \int_\Gamma \sigma_o m_\alpha j_\alpha d\Gamma \quad (5)$$

for all kinematically associated fields, v_i , $\dot{\epsilon}_{kl}$, and j_α , which are material velocity, strain rate, and flow rate, respectively. Greek subscripts (α)

have the range 1, 2 (repeated indices represent the summation) and refer to a local set of cartesian coordinates in the grain boundary. In addition, ' T_i ', ' $\omega(\dot{\epsilon}_{kl})$ ', and ' A_{gb} ' represent tractions, stress power rate, and the grain boundary surface. As shown in Fig. 6, ' m ' is the unit normal vector to the arc (' Γ ', see Fig. 2) of the intersection of the grain boundary and the cavity surface, and ' σ_o ' is the normal stress at the cavity tip (stress component normal to the grain boundary), respectively. The last term in Eq. (5) comes from the condition of continuity of the chemical potential at the cavity tip.

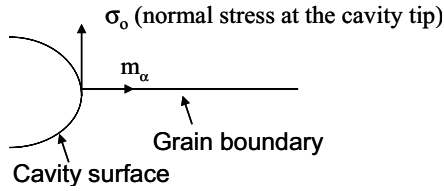


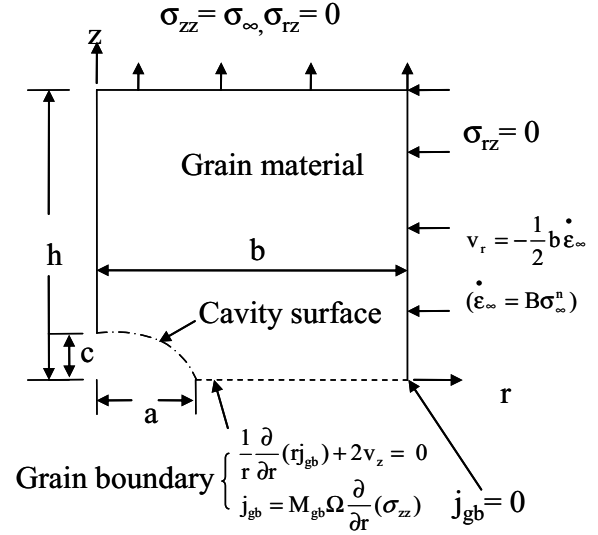
Figure 6: Sintering stress (σ_o) and the unit normal vector (m_α) at the cavity tip.

In order to have a bounded flux at the cavity tip, the chemical potential must be continuous at the cavity tip. Therefore, the normal stress at the cavity tip (' σ_o '), which is known as the sintering stress of the cavity, is a function of the specific surface tension (' γ_s ') and cavity principal curvatures at the cavity tip (' κ_1 and κ_2 ' shown in Fig. 2) as follows.

$$\sigma_o = \gamma_s(\kappa_1 + \kappa_2). \quad (6)$$

A cylinder containing a cavity at the center as shown in Fig. 7 represents the unit cell model for FE analysis. The material is assumed to be incompressible, and this leads to the velocity boundary condition on the outer boundary of the cylinder ($r = b$). Due to the symmetric geometric condition, only one quarter of the unit cell is sufficient for the analysis. The far-field stress state is assumed to be uniaxial. The remote creep strain rate in the z -direction is represented by ' $\dot{\epsilon}_\infty$ ', and the corresponding remote stress in the z -direction is denoted by ' σ_∞ '.

In this analysis, the grain material is assumed to be elastic and non-linear viscous, with the nonlin-



Boundary conditions on the grain boundary

$$\frac{1}{r} \frac{\partial}{\partial r} (r j_{gb}) + 2v_z = 0: \text{matter conservation law}$$

$$j_{gb} = M_{gb} \Omega \frac{\partial}{\partial t} (\sigma_{zz}): \text{linear kinetic law for atomic flux}$$

σ_o is specified at $r = a$: the continuous chemical potential condition

$$j_{gb} = 0 \text{ at } r = b: \text{axis-symmetric condition}$$

Boundary conditions on the outer surface

$$\text{On } z = h: \sigma_z = \sigma_\infty, \sigma_{rz} = 0$$

$$\text{On } r = b: \sigma_{zr} = 0, v_r = -\frac{1}{2} \dot{\epsilon}_\infty b$$

$$\text{On } r = 0: u_r = 0$$

Figure 7: Unit cell model with a spherical-cap shaped cavity with the major radius ' a ', the minor radius ' c ', and the cavity half distance ' b '. The boundary conditions on the grain boundary satisfy the linear kinetic law for the atomic flux and the matter conservation law. The boundary conditions on the outer surface of the grain material satisfy the axis-symmetric condition.

ear creep specifically of the power law form

$$\sigma = \Lambda \dot{\epsilon}^{1/n} \quad (7)$$

in the uniaxial tension where ' Λ ' and ' n ' are material constants. Following Needleman and Rice (1980), we consider an incremental form of a

functional, $\Delta\bar{F}_{gb}$, given by

$$\Delta\bar{F}_{gb} = \int_V \boldsymbol{\sigma} : \Delta\mathbf{d}dV - \int_{S_T} \mathbf{T} \cdot \Delta\mathbf{v}dS + \int_{A_{gb}} \frac{1}{2M_{gb}\Omega} \Delta\mathbf{j} \cdot \Delta\mathbf{j}dA + \int_{\Gamma} \sigma_o \mathbf{m} \cdot \Delta\mathbf{j}d\Gamma \quad (8)$$

for all kinematically associated fields, the rate of deformation tensor, ' \mathbf{d} ', the velocity, ' \mathbf{v} ', and the volumetric flux, ' \mathbf{j} '.

Based on the matter conservation law, the incremental volumetric flux crossing the unit length in the grain boundary, ' Δj_{gb} ', are related to the incremental grain boundary velocity, ' Δv_N '. Due to the axis-symmetric nature of problem, the relevant components of the flux and velocity, respectively, reduce to ' Δj_r ' and ' Δv_z '.

$$\Delta j_{gb} = \Delta j_r = \frac{2}{r} \int_r^b r' \Delta v_z(r', z=0) dr' \quad (9)$$

Using the above equation, the last two terms of the functional becomes,

$$\Delta\bar{F}_d = \frac{4\pi}{M_{gb}\Omega} \int_a^b \frac{1}{r} \left(\int_r^b r' \Delta v_z(r', 0) dr' \right)^2 dr + 4\pi\sigma_o \int_a^b r' \Delta v_z(r', 0) dr' \quad (10)$$

In this work, linear shape functions are employed for the incremental normal velocities as follows.

$$\Delta v_z = \sum_{i=1}^N \Phi_i(r) \Delta v_{zi} \quad (11)$$

where

$$\begin{aligned} \Phi_i(r) &= \frac{r - r_{i-1}}{r_i - r_{i-1}} \quad \text{for } r_{i-1} \leq r \leq r_i \\ \Phi_i(r) &= \frac{r_{i+1} - r}{r_{i+1} - r_i} \quad \text{for } r_i \leq r \leq r_{i+1} \\ \Phi_i(r) &= 0 \quad \text{for } r < r_{i-1} \text{ or } r > r_{i+1} \end{aligned} \quad (12)$$

and ' N ' and ' Δv_{zi} ' are the total number of nodal points and the incremental nodal velocity at point ' i '.

After some algebraic manipulations, $\Delta\bar{F}_d$ becomes

$$\Delta\bar{F}_d = \sum_{i=1}^N \sum_{j=1}^N C_{ij} \Delta v_{zi} \Delta v_{zj} + \sum_{i=1}^N p_i \Delta v_{zi} \quad (13)$$

where the stiffness matrix ' C_{ij} ' and ' p_i ' are given by,

$$C_{ij} = \frac{4\pi}{M_{gb}\Omega} \int_a^b \frac{1}{r} g_i(r) g_j(r) dr \quad (14)$$

$$p_i = 4\pi\sigma_o g_i(a)$$

with

$$g_i(r) = \int_r^b r' \Phi_i(r') dr' \quad (15)$$

Numerical integration is performed to evaluate the components ' C_{ij} ' and ' p_i '. The stiffness matrix from the functional (8) is constructed and then the effect of creep flow along the grain boundary on the grain boundary diffusion is analyzed numerically. The cavity growth rate is calculated for the given stress (' σ_∞ '), grain boundary mobility (' M_{gb} ', see Eq. (4)), cavity tip geometry (' k_1 and ' k_2 ', see Fig. 2), and material constitutive relation, Eq. (7). The solution of this problem gives two results: the diffusive flux (' j_o ') at the cavity tip and the velocity of nodes along cavity surface due to "jacking" effect and viscoplastic deformation of the surrounding material.

2.2 Finite Difference Form

For the second step in the solution process, the cavity evolution due to the surface diffusion is solved. As discussed earlier, Needleman and Rice (1980) assumed that a spherical cavity shape was maintained during the cavity growth for the grain boundary diffusion controlled problem. However, experimental results (Goods and Nix (1978) and Raj (1978)) have shown that the shape of a cavity becomes a crack rather than a sphere under the surface diffusion controlled condition. Therefore, an analysis, which includes the surface diffusion process, will produce physically more general results than the problems analyzed by Needleman

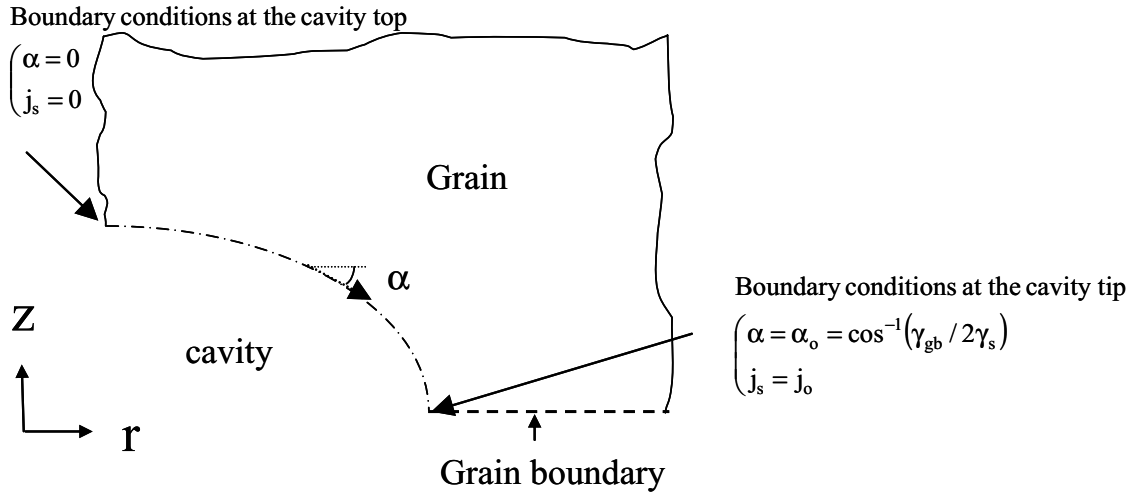


Figure 8: Boundary conditions along the cavity surface for the finite difference method.

and Rice (1980). In this numerical procedure, the cavity profile will be updated at each time step, satisfying boundary conditions.

Figure 8 shows the axis-symmetric spherical-shaped cavity with boundary conditions at the cavity top and the cavity tip. Due to the symmetry, only one quarter of the cavity is sufficient for the cavity evolution simulation. At the cavity top, the atomic flux, ‘ j_s ’, and the angle, ‘ α ’, are zero because of the symmetry condition. At the cavity tip, the angle, ‘ α_o ’ (see Fig. 4) between the cavity surface and grain boundary remains unchanged to maintain the local force equilibrium condition. In addition, the cavity tip flow, ‘ j_s ’, is the same as the flow to grain boundary, ‘ j_o ’. Following the numerical simulations by Martinez and Nix (1982), the cavity tip node moves freely to satisfy this boundary condition. The four boundary conditions imposed for the cavity evolution are:

$$\begin{cases} \alpha = 0 \\ j_s = 0 \end{cases} \quad \text{at the cavity top}$$

$$\begin{cases} \alpha = \alpha_o = \cos^{-1}\left(\frac{\gamma_{gb}}{2\gamma_s}\right) \\ j_s = j_o \end{cases} \quad \text{at the cavity tip}$$

(16)

For a given step time, the cavity shape evolves in a manner satisfying the matter conservation law and the above boundary conditions.

From Eqs. (1)₁, (2)₁, and (3)₁, the atomic flow

driven by the chemical potential difference along cavity surface, ‘ j_s ’, is

$$j_s = M_s \Omega \gamma_s \frac{d(\kappa_1 + \kappa_2)}{dS} \quad (17)$$

where ‘ dS ’ is the surface arc element in the direction of the flux. The diffusive flux (‘ j_o ’) at the cavity tip is given from the previously discussed finite element portion of the analysis. The cavity surface velocity, ‘ v_N ’, is determined from the matter conservation law as follows.

$$v_N = \frac{1}{r} \frac{d(j_s r)}{dS} \quad (18)$$

Equations (18) and (19) are the kinetic equations which can describe cavity evolution.

The basic numerical scheme of the finite difference method is used to calculate the movement of each point on the cavity surface satisfying the matter conservation law along the cavity surface. Figure 9 shows total ‘ n ’ discrete points along the cavity surface. Point ‘1’ is located at the cavity top and point ‘ n ’ is at the cavity tip. The direction of positive arc length ‘ S ’ is also shown.

Figure 10 and 11 show the definition of the normal direction of each node. It is necessary to calculate the principal curvatures and the atomic flux to obtain the velocity at each node. The ‘ i^{th} ’ point on the cavity surface has coordinates ‘ $(r_i(t), z_i(t))$ ’ at time t . The normal direction at a node is constructed geometrically as the line passing the node

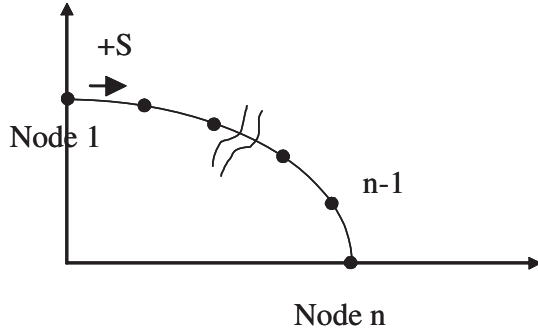


Figure 9: Discretized cavity surface is schematically represented, which is used in the finite difference method.

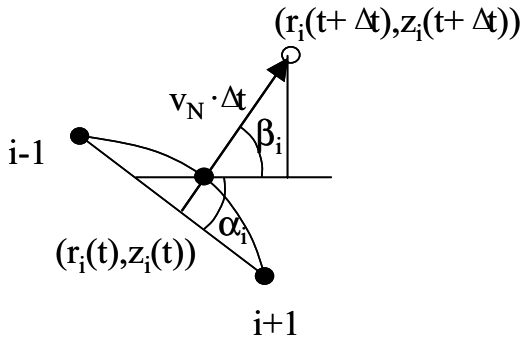


Figure 10: Finite difference numerical scheme showing how the i^{th} point on the cavity surface moves to the new position (hollow point) after time increment Δt and the definition of the angle β_i .

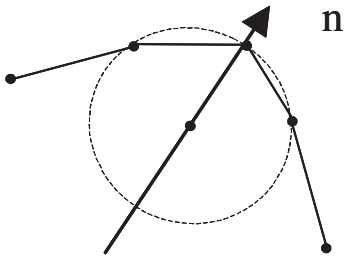


Figure 11: Definition of the surface normal vector (\mathbf{n}) at the node on the cavity surface.

and center of circle, which passes ' $i-1^{th}$ ', ' i^{th} ', and ' $i+1^{th}$ ' nodes.

The first primary curvature ' κ_1 ' is chosen to be in the plane of the figure and it is approximated to be the same as the inverse of the radius of the inscribed circle. The sign of the curvature is positive when the center of circle is inside the cavity and negative when it is outside. The second primary curvature is given by

$$(\kappa_2)_i = \frac{\cos \beta_i}{r_i} \quad (19)$$

on the assumption of the axis-symmetric geometry, where angle ' β_i ' is described on Fig. 10.

The atomic flux at the ' i^{th} ' point is obtained by Eq. (17) using the finite difference method

$$(j_s)_i = M_s \Omega \gamma_s \frac{[(\kappa_1 + \kappa_2)_i - (\kappa_1 + \kappa_2)_{i-1}]}{[\Delta S]_{i-1}^i} \quad (20)$$

where ' $[\Delta S]_{i-1}^i$ ' represents the distance between ' i^{th} ' point and ' $i-1^{th}$ ' point. Differentiation of Eq. (18) gives the more detailed form of displacement velocity :

$$v_N = \left(\frac{dj_s}{dS} + \frac{j_s}{r} \sin \beta \right). \quad (21)$$

Using the open ended finite difference method, the above equation can be approximated as

$$(v_N)_i = \left(\frac{(j_s)_{i+1} - (j_s)_i}{[\Delta S]_i^{i+1}} + \frac{(j_s)_i}{r_i} \sin \beta_i \right) \quad (22)$$

where ' $[\Delta S]_i^{i+1}$ ' is the distance between ' i^{th} ' point and ' $i+1^{th}$ ' point. In the above equation, ' $(v_N)_i$ ' is obtained by using ' $(j_s)_i$ ' and ' $(j_s)_{i+1}$ ', where ' $(j_s)_i$ ' is obtained from the curvatures at ' i^{th} ' point and ' $i-1^{th}$ ' point and the distance between these two points. Normal velocity representation, Eq. (22), is centralized since information from ' $i-2^{th}$ ', ' $i-1^{th}$ ', ' i^{th} ', ' $i+1^{th}$ ', and ' $i+2^{th}$ ' feeds into Eq. (22). The normal velocity is calculated from Eq. (22) and the normal direction is also obtained from the geometric information at each point on the cavity surface.

An appropriate time increment ' Δt ', which depends on the flux at the cavity tip, is chosen. The

points on the cavity surface moves by an amount ' $v_N \Delta t$ ' to its new coordinates, which are approximated as

$$\begin{aligned} r_i(t + \Delta t) &= r_i(t) + (v_N)_i \Delta t \cos \beta_i \\ z_i(t + \Delta t) &= z_i(t) + (v_N)_i \Delta t \sin \beta_i \end{aligned} \quad (23)$$

All points along the cavity surface moves in a manner based on the scheme described above.

The 1st and n^{th} points (the points at the cavity top and at the cavity tip), however, move differently because of the boundary conditions. First, the point at the cavity top moves to satisfy the two boundary conditions, the angle $\beta = \pi/2$ and the flux $(j_s)_1 = 0$. Since $\beta = \pi/2$ from the geometric symmetry boundary condition, it is reasonable to set an imaginary node by reflecting point 2 across the z-axis to calculate ' κ_1 ' at cavity top. The second primary curvature ' κ_2 ' is the same as ' κ_1 ' due to the axis-symmetric cavity geometry i.e. $(\kappa_2)_1 = (\kappa_1)_1$. When $r = 0$, the matter conservation requires that $v_N = 2 \frac{dj_s}{ds}$ and it can be approximated by

$$(v_N)_1 = 2 \left(\frac{(j_s)_2 - (j_s)_1}{[\Delta S]_1^2} \right). \quad (24)$$

The other end point, the ' n^{th} ' point, should move along the r-axis satisfying the local tension equilibrium. Therefore, the velocity calculation according to Eq. (22) is not attempted for this point. Instead, after the ' $n - 1^{\text{th}}$ ' point moves to a new position, the ' n^{th} ' point floats to a new position in order to satisfy the surface tension equilibrium. It is based on the physical phenomenon that the atoms near the cavity tip instantaneously move to satisfy the local surface tension. The distance between the ' n^{th} ' and ' $n - 1^{\text{th}}$ ' point was kept within ' $0.1a_I$ ' where ' a_I ' is the initial void radius. This guarantees that both the equilibrium condition of surface tension at the cavity tip and the cavity growth rate are accurately predicted throughout the numerical simulation. The flux at the ' n^{th} ' point, ' $(j_s)_n$ ', is set equal to ' j_o ' obtained from the finite element analysis and that is used to calculate velocity of ' $n - 1^{\text{th}}$ ' point, ' $(v_N)_{n-1}$ ' as in Eq. (22).

By trial and error, it was found that 15 points, which are equally spaced along the cavity surface,

are sufficient for an accurate analysis. If ' $\Delta\beta$ ' exceeds 18° , a new node is inserted to reduce ' $\Delta\beta$ ', while the point is removed if ' $\Delta\beta$ ' becomes less than 2° . This procedure reduces the number of points at low curvature regions and increases the number of points at high curvature regions. In addition, ' $[\Delta S]_i^{i+1}$ ' is restricted not to become too large in the region of high curvature. The time increment ' Δt ' is limited so that the cavity radius increment ' Δa ' does not exceed ' $0.005a_I$ '.

The proposed numerical method provides a physically based cavity growth rate where two important aspects of the cavity growth mechanism are considered. First, it includes the effect of the viscoplastic material deformation on the single cavity growth. Second, the cavity profile is updated so that the physical boundary conditions such as the matter conservation law, equilibrium dihedral angle, and continuous chemical potential condition are satisfied. In section 3.1 and 3.2, the proposed numerical method is verified for two extreme cases; grain boundary diffusion controlled cavity growth and surface diffusion controlled cavity growth. In section 3.3 and 3.4, cavity shape evolution of an initial spherical cavity is numerically analyzed and cavity growth predictions using the current numerical method are compared with experimental results.

3 Results

3.1 Modeling of Grain Boundary Diffusion Controlled Cavity Growth

When the surface diffusion is very fast, the grain boundary diffusion controls cavity growth and the spherical-shaped cavity maintains its original shape while it grows. Based on these assumptions, Needleman and Rice (1980) calculated cavity growth rates and final rupture time of a spherical-shaped cavity. Chen and Argon (1981) proposed an approximate cavity growth equation, which reproduces the Needleman and Rice (1980) numerical results within an error of 30%. In the following, grain boundary diffusion controlled cavity growth is calculated using the current numerical methods, and we verify the proposed numerical method by comparing the obtained result

with the work by Needleman and Rice (1980) and that by Chen and Argon (1981).

In this study, numerical analysis of an initial spherical-shaped cavity was carried out for $a_I/b = 0.1$ and $a_I/L = 0.316$, where ‘ L ’ is defined by

$$L = \left(\frac{M_{gb} \sigma_{\infty} \Omega}{\dot{\epsilon}_{\infty}} \right)^{\frac{1}{3}}. \quad (25)$$

The parameter ‘ L ’ is introduced by Rice (1979) and it physically represents “effective diffusion length”. When the effective diffusion length ‘ L ’ is smaller than the cavity half-distance ‘ b ’, it is approximately assumed that atoms diffuse from the cavity tip to ‘ L ’ instead of diffusing from the cavity tip to ‘ b ’. Chen and Argon (1981) considered the “effective diffusion length” effect in the cavity growth rate equation. The equilibrium dihedral angle was chosen to be 70° and the creep exponent was taken to be 4.5. These conditions are the same as those used by Needleman and Rice (1980). In order to reproduce fast surface diffusion assumption employed by Needleman and Rice (1980), a large value of diffusivity ratio, $D_s/D_{gb} = 171$, is chosen in this numerical simulation.

In Fig. 12(a) and (b), the nondimensionalized cavity radius, ‘ a/b ’, is plotted as a function of nondimensionalized time ‘ $t\dot{\epsilon}_e^{cr}$ ’, where ‘ $\dot{\epsilon}_e^{cr}$ ’ is the equivalent creep strain rate. Proposed numerical results with or without jacking effect are compared with the work by Needleman and Rice (1980) and those by Chen and Argon (1981). Cavity growth rates by Needleman and Rice (1980) are only available for $a/b = 0.1, 0.33, \text{ and } 0.67$. Therefore, the cavity growth rate for other ‘ a/b ’ values are obtained by the interpolation method suggested by Needleman and Rice (1980). Although they proposed an extrapolation method to calculate cavity growth rates for $a/b > 0.67$, it was not used here.

From Fig. 12, it is clear that the proposed numerical method exactly reproduces Needleman and Rice (1980) result by choosing a large surface diffusivity. In addition, it also demonstrates that the assumption of the maintenance of the spherical cavity shape during the growth (which is em-

ployed by Needleman and Rice (1980)) is valid under the fast-surface diffusion condition. The proposed unified numerical method can simulate cavity growth by considering only atomic diffusion contribution (denoted as \dot{V}_1) to the total cavity volume ($\dot{V}_{tot} = \dot{V}_1 + \dot{V}_2$) increase. When the cavity volume increase rate due to ‘jacking’ and deformation (denoted as \dot{V}_2) is not included, the present model overestimates cavity coalescence time. Needleman and Rice (1980) pointed out the importance of cavity shape change due to ‘jacking’ and deformation. The analysis with and without this effect quantitatively demonstrates the importance of \dot{V}_2 contribution. The result by Chen and Argon (1981) shows significant deviation from those by Needleman and Rice (1980) and by the proposed model in $t\dot{\epsilon}_e^{cr} > 0.2$. This deviation may be attributed to their assumption that the grain boundary displacement (‘jacking’ effect) due to matter flow is constant over diffusion distance ‘ L ’.

Figure 13 shows nondimensionalized cavity volume growth rates, ‘ $\dot{V}/(\dot{\epsilon}_e^{cr} a_I^3)$ ’, as a function of nondimensionalized cavity radius ‘ a/b ’. Cavity volume growth rates predicted by the current numerical method match well with the Needleman and Rice (1980) numerical result at $a/b = 0.1, 0.33, \text{ and } 0.67$. Chen and Argon (1981) equation underestimates cavity volume growth rate when $a/b > 0.5$ under the assumption of fast surface diffusivity.

As opposed to the work by Needleman and Rice (1980), the continuous cavity growth is numerically predicted. Only the initial cavity radius is required in the present work. One to one match between our simulation and the results by Needleman and Rice (1980) demonstrates the validity of the approach provided here.

3.2 Modeling of Surface Diffusion Controlled Cavity Growth

When surface diffusion controls cavity growth, the cavity tends to elongate in the direction normal to the applied stress and the cavity shape also tends to become crack-like. In the following, surface diffusion controlled cavity growth is calculated using the fully-coupled numerical method

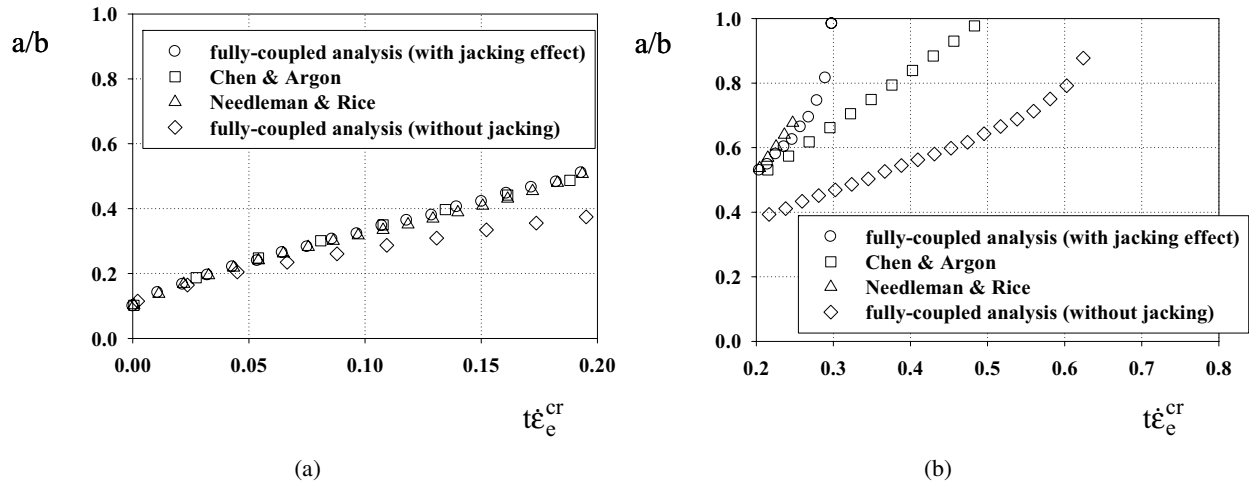


Figure 12: (a) Nondimensionalized cavity major radius as a function of nondimensionalized time for $a_I/L = 0.316$, $a_I/b_I = 0.1$, and $D_s/D_{gb} = 171$ (fast surface diffusion). When a/b is $0 \sim 0.5$, the present numerical results (with jacking effect) reproduce the Needleman and Rice results. In this range, the Chen and Argon results also match with the Needleman and Rice results. When jacking effect is not considered, present result deviates with the other three results. That implies jacking effect is significant in this a/L range. (b) Nondimensionalized cavity major radius as a function of nondimensionalized time for $a_I/L = 0.316$, $a_I/b_I = 0.1$, and $D_s/D_{gb} = 171$ (fast surface diffusion). When a/b is $0.5 \sim 1.0$, the present results still match well with the Needleman and Rice results. However, Chen and Argon result starts to deviate from the Needleman Rice results.

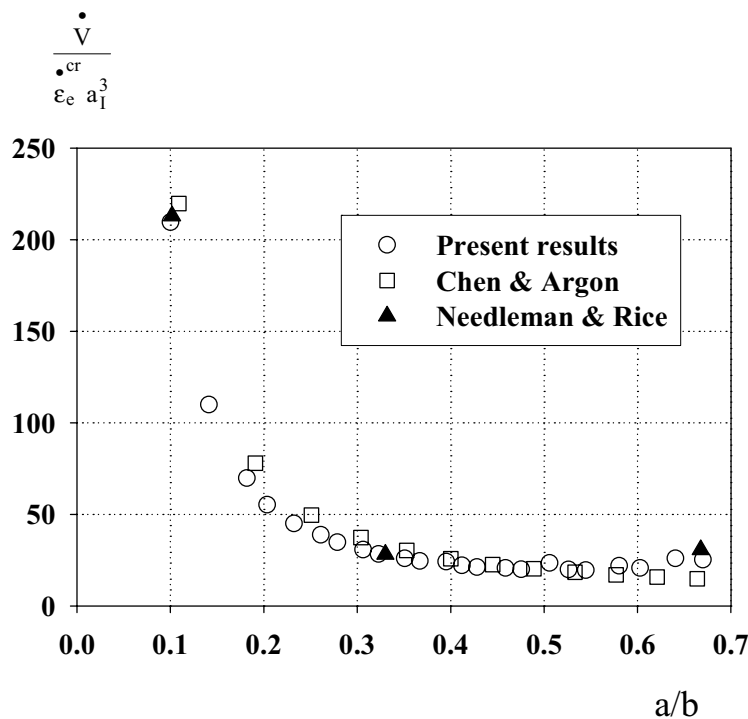


Figure 13: Nondimensionalized cavity volume growth rate as a function of nondimensionalized cavity major radius for $a_I/L = 0.316$, $a_I/b_I = 0.1$, and $D_s/D_{gb} = 171$ (fast surface diffusion). Present results match well with the Needleman and Rice results (reported at $a/b = 0.1, 0.33$, and 0.66). Chen and Argon results start to deviate when a/b is larger than 0.5 .

and we verify our approach against the results by Martinez and Nix (1982) and Chuang et al. (1979).

For this purpose, we use the same parameters as in Martinez and Nix (1982). The diffusivity ratio is expressed as

$$f = \frac{D_{gb}}{D_s}. \quad (26)$$

Nondimensionalized time and nondimensionalized stress are given by

$$T = \frac{t}{a_I^4 / M_s \Omega \gamma_s} \quad (27)$$

$$\Sigma = \frac{\sigma a_I}{\gamma_s}. \quad (28)$$

In order to compare the results from the current fully-coupled method to those from the previous works (Martinez and Nix (1982), Chuang et al. (1979)), where the material deformation is not considered, the remote normal stress is set to be small so that the resulting viscoplastic deformation is negligible. The ratio of the applied normal stress to Young's modulus, σ_∞/E , is chosen to be 10^{-4} and initial ' a_I/b_I ' is 0.1. The capillarity angle at cavity tip is assumed to be 70° and the creep exponent is taken to be 4.5.

In Fig. 14, a log-log plot of the nondimensionalized rupture time vs. nondimensionalized applied stress is shown. For $f = 1$ and $f = 10$ (surface diffusion controlled region), the current numerical results agree well with the results of Martinez and Nix (1982) (denoted as M & N) and Chuang et al. (1979) (denoted as C & R). In reality, the f values of most metals do not exceed 10.

Martinez and Nix (1982) reported stress exponents for fracture, which is the slope of the Fig. 14, as -1.7 and -2.2 for $f = 1$ and $f = 10$, respectively. The corresponding values based on the proposed methods are determined to be -1.69 and -2.19 for $f = 1$ and $f = 10$, respectively. These analyses are performed here in the region where the creep deformation is of second order importance. However, the small differences between these values can be attributed to the creep effect, which is automatically included in the proposed method.

Since the proposed method is fully coupled, the sintering stress (the normal stress at the cavity tip) and the stress along the grain boundary can be calculated including the viscoplastic deformation. In addition, this detailed stress distribution can be continuously monitored as the cavity changes its shape. Figure 15 shows the stress distribution along the grain boundary when $a/b = 0.1, 0.3, 0.5, 0.7,$ and 0.9 for $f = 1$ and $f = 10$, respectively. $f = 10$ implies more surface diffusion controlled than $f = 1$ as in Eq. (26). The normal stress along the grain boundary increases as the cavity grows for both cases ($f = 1$ and $f = 10$) since the grain boundary area decreases. For $f = 10$, the sintering stress (σ_o), increases as the cavity grows. For $f = 1$, the sintering stress decreases when $a = 0.3$ and 0.5 . As shown in Eq. (6), the sintering stress is proportional to the summation of the two curvatures (κ_1 and κ_2). Therefore, the difference between the sintering stress for $f = 1$ and $f = 10$ reflects the difference in the cavity surface geometry near the tip, which can be further analyzed as follows.

Since a cavity becomes crack-like as it grows for both cases ($f = 1$ and $f = 10$), the first primary curvature (κ_1) increases at the cavity tip. The second primary curvature (κ_2), which is calculated according to Eq. (19), decreases as the radius increases. For $f = 10$, the sintering stress increases as the cavity grows because the increase of the first primary curvature is dominant compared to the decrease of the second primary curvature. However, for $f = 1$, the decrease of the second primary curvature (κ_2) leads to sintering stress decrease when $a = 0.3, 0.5$. These analyses imply that the cavity shape for $f = 10$ becomes sharper than that for $f = 1$. This point is clearly demonstrated by continuously monitoring the cavity shape change. Figure 16(a) and (b) show the cavity shape when $a = 0.1, 0.3, 0.5,$ and 0.7 for $f = 1$ and $f = 10$, respectively. Figure 16 clearly demonstrates that the cavity shape for $f = 10$ becomes sharper than that for $f = 1$. The nodal points on the cavity surface were marked along the cavity surface. Initially, 15 nodes are used along the cavity surface with the same separation distance. As the cavity shape becomes

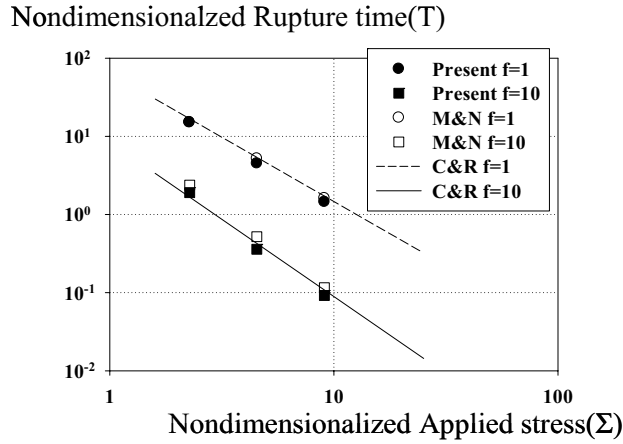


Figure 14: Nondimensionalized grain boundary rupture time (when a/b reaches to 1) vs. nondimensionalized applied stress under different diffusivity ratios ($f = D_{gb}/D_s$), for $a_l/b_l = 0.1$, $\sigma_\infty/E = 10^{-4}$, and cavity tip angle $=70^\circ$. Chuang et al. (1979) (C & R) analytically calculated surface diffusion controlled cavity growth rate on the assumption of crack-like cavity. Martinez and Nix (1982) (M & N) used Finite Difference Method to evaluate the cavity shape evolution. When $f = 1$ and 10 (surface diffusion controlled region), the present results match well with both M & N and C & R.

more crack-like, additional nodal points are automatically created along the high curvature area based on the nodal ‘removal-creation’ algorithm employed in this work.

As opposed to the work by Martinez and Nix (1982), the cavity coalescence time is numerically obtained with the deformation consideration. One to one match between our simulation and the results by Martinez and Nix (1982) and Chuang et al. (1979) demonstrates that our approach is valid for the simulation of the surface diffusion dominant cavity growth.

Due to fully coupled nature of our method, the detailed stress distribution including the deformation can be analyzed as shown in Fig. 15. In practical applications, an applied remote load does not remain constant, which can change grain boundary stability. The detailed stress analysis as in Fig. 15 will be crucial in predicting grain boundary

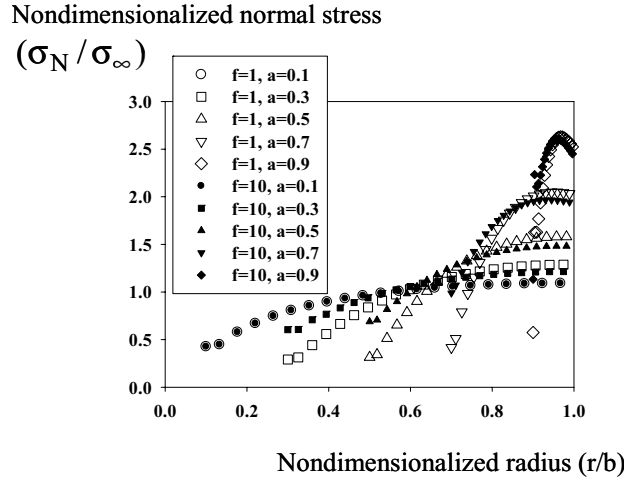


Figure 15: The nondimensionalized normal stress of each element above the grain boundary vs. the nondimensionalized grain boundary length is shown for $\sigma_\infty/E = 10^{-4}$ and cavity tip angle 70° . When $a/b = 0.1$, stress distribution is the same for both $f = 1$ and $f = 10$ (surface diffusion controlled) cases. The stress along the grain boundary increases as the cavity grows for both cases, $f = 1$ and $f = 10$, since the grain boundary area decreases. For $f = 10$, the sintering stress (σ_o), which is the normal stress at the cavity tip, increases as the cavity grows. For $f = 1$, the sintering stress decreases when $a = 0.3$ and 0.5.

rupture without cavity coalescence.

3.3 Transition from quasi-equilibrium mode to crack-like mode

Based on the results from section 3.1 and 3.2, the proposed numerical model is validated against two extreme cases; grain boundary and surface diffusion controlled cavity growth cases. In section 3.2, the continuous cavity shape change is monitored, but the viscoplastic deformation effect on the cavity growth is not included. Since the viscoplastic deformation effects on the cavity volume growth rate is important in the deformation enhanced diffusion regime as shown in section 3.1, it is necessary to study the cavity shape change while considering creep deformation. In this section, we perform analyses in regimes where both surface diffusion and deformation enhanced grain boundary diffusion are im-

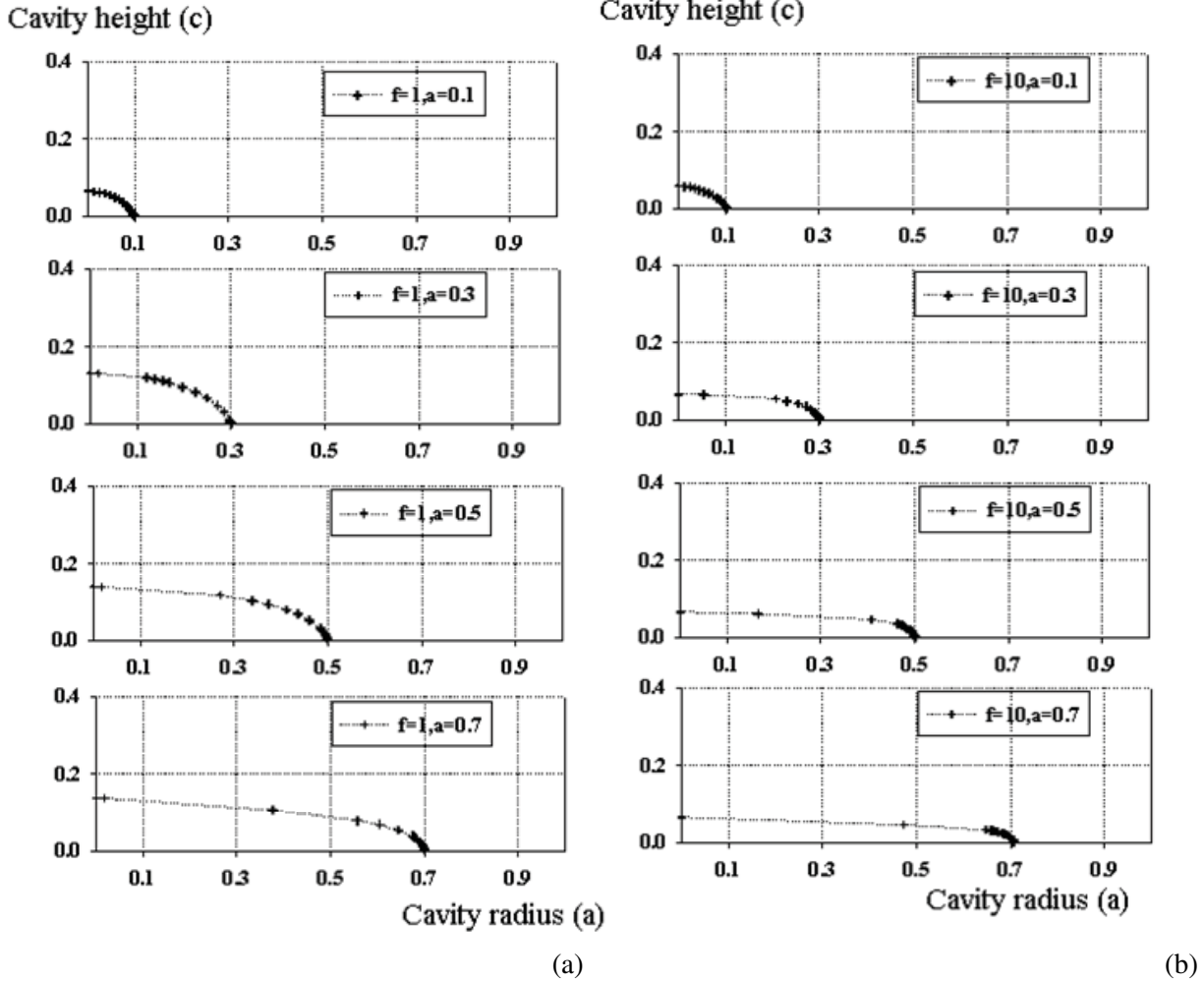


Figure 16: Evolution in the cavity shape for $\sigma_\infty/E \approx 10^{-4}$ and cavity tip angle 70° , (a) $f = 1$ (surface diffusion controlled), (b) $f = 10$ (more surface diffusion controlled case). In all cases $a_1/b_1 = 0.1$ and the cavity changes to crack-like. The node removal-creation procedure is clearly shown for both cases. Cavity shape becomes more crack-like when $f = 10$.

portant.

In order to include the effect of the material viscoplastic deformation on the cavity growth, the remote normal stress is set to be large so that the ratio between the initial cavity radius, a_1 , and the effective grain boundary diffusion length, L , is larger than 0.1. Three different (a_1/L) ratios, 0.1, 0.316, and 1.0, are chosen, and the grain boundary and surface diffusivity are chosen so that the cavity is subjected to shape change. Previously Chen and Argon (1981) successfully calculated the cavity radius growth rate in this regime based on the assumed (spherical or crack-like) cavity shape. As opposed to their work (Chen and Argon

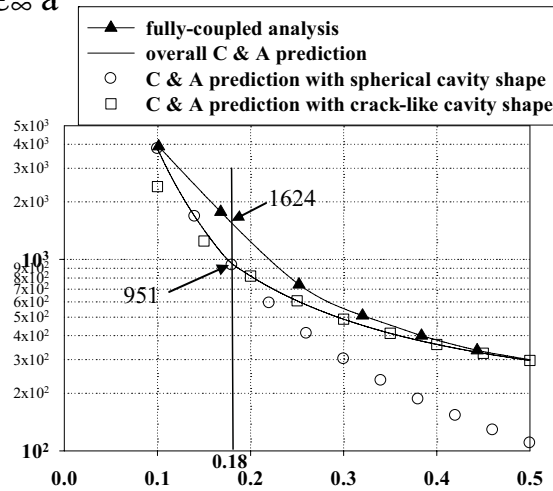
(1981)), in the proposed fully-coupled method, the cavity shape is determined as a result of the numerical simulation. In order to examine the effect of continuous cavity shape change on the cavity growth rate, we organize our numerical results using the same nondimensional parameter α , defined by

$$\alpha = \left(\frac{4\pi h(\psi)}{(4 \sin(\frac{\psi}{2}))^{\frac{3}{2}}} \right) \times \left(\left(\frac{D_{gb}}{D_s} \right) \left(\frac{\sigma_\infty L}{\gamma_s} \right) \right)^{\frac{1}{2}}, \quad (29)$$

as in the work by Chen and Argon (1981) where $h(\psi) = V/(4\pi a^3/3) =$

Nondimensionalized cavity growth rate

$$4\pi h(\psi) \frac{da}{dt} / \epsilon_{\infty} a$$

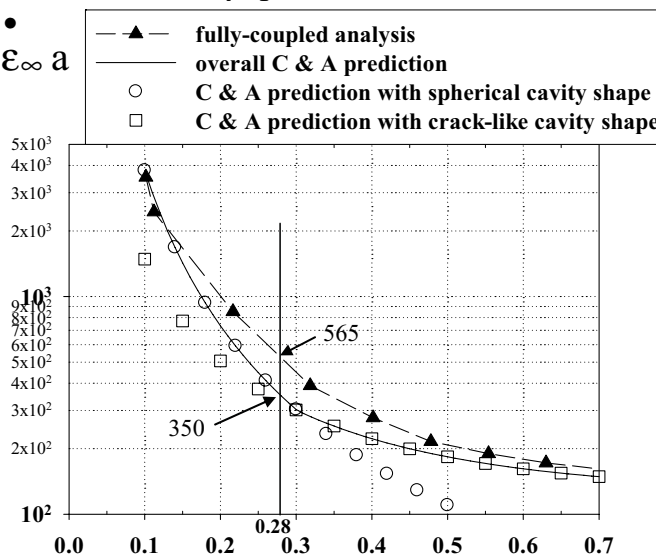


Nondimensionalized cavity radius (a/L)

Figure 17: Nondimensionalized cavity growth rate vs. nondimensionalized cavity radius is shown for $a_1/L = 0.1$ and $\alpha = 16.2$. An initial spherical cavity evolves to a crack like cavity with much higher da/dt values compared to the prediction by Chen and Argon (1981); the maximum difference occurs when $a/L = 0.18$, where the current result predicts 1624 and the analysis by Chen and Argon (1981) predicts 951.

Nondimensionalized cavity growth rate

$$4\pi h(\psi) \frac{da}{dt} / \epsilon_{\infty} a$$



Nondimensionalized cavity radius (a/L)

Figure 18: Nondimensionalized cavity growth rate vs. nondimensionalized cavity radius is shown for $a_1/L = 0.1$ and $\alpha = 10.0$. An initial spherical cavity evolves to a crack like cavity with much higher da/dt values compared to the prediction by Chen and Argon (1981); the maximum difference occurs when $a/L = 0.28$, where the current result predicts 565 and the analysis by Chen and Argon (1981) predicts 350.

Nondimensionalized cavity growth rate

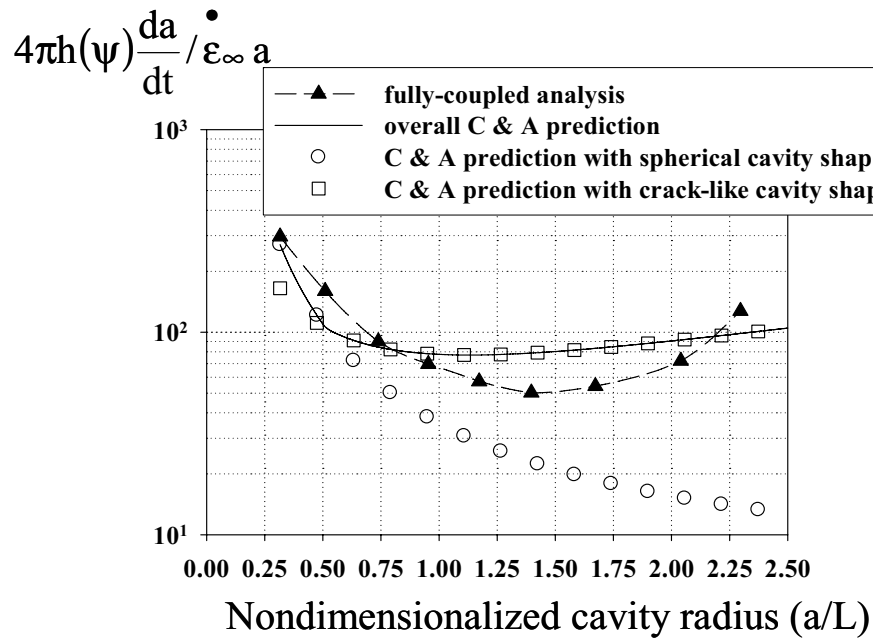


Figure 19: Nondimensionalized cavity growth rate vs. nondimensionalized cavity radius is shown for $a_1/L = 0.316$ and $\alpha = 5.82$. Initial nondimensionalized cavity growth rates predicted by the fully-coupled method are slightly higher than those by Chen Argon (1981). As a/L increases, cavity growth rates do not follow those based on the assumed cavity shape.

Nondimensionalized cavity growth rate

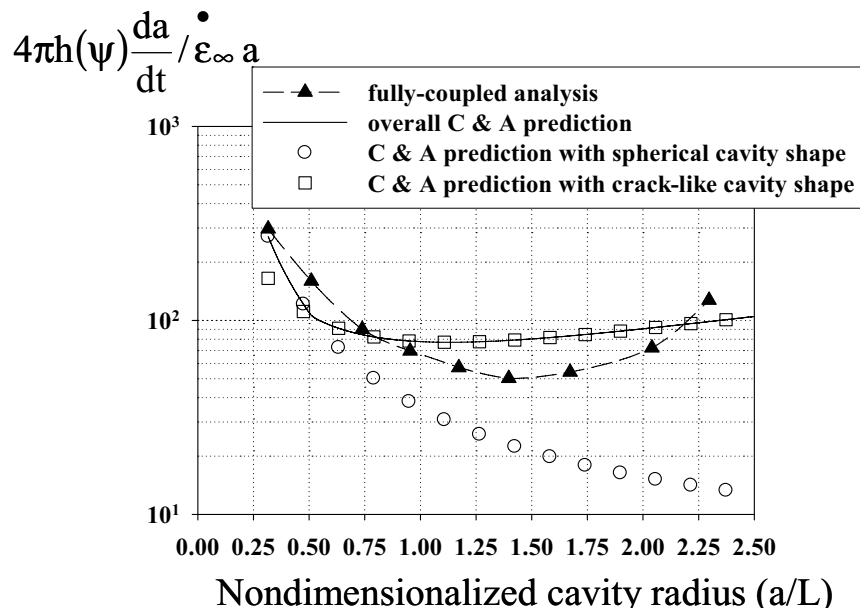


Figure 20: Nondimensionalized cavity growth rate vs. nondimensionalized cavity radius is shown for $a_1/L = 1.0$ and $\alpha = 1.0$. Since the cavity volume change due to creep flow (jacking effect and the cavity shape change due to creep flow) is significant in this a/L range, the analysis by Chen and Argon (1981), which assumes that the cavity volume growth rate is all related with the atomic flow rate at cavity tip, can not accurately predict the cavity major radius rate and cavity shape change.

$$(1/(1 + \cos \psi) - \cos \psi/2) / \sin \psi.$$

Figure 17~20 show the nondimensionalized cavity growth rate vs. the nondimensionalized cavity radius for various cases. In order to properly model the cavity shape transition from the spherical to the crack-like, the smaller α , which means higher surface diffusivity, is chosen for the higher a/L values. The cavity growth rate predictions based on the spherical cavity shape assumption, the crack-like cavity shape assumption, and the sphere and crack-like combined assumption by Chen and Argon (1981) are included for the comparison purpose.

In Fig. 17 ($a_I/L = 0.1$ and $\alpha = 16.2$), the overall cavity growth rate predicted by the fully-coupled method is larger than that by Chen and Argon (1981) prediction. The maximum difference occurs at $a/L = 0.18$, where the proposed method predicts 1624 and the result by Chen and Argon (1981) predicts 951, and the ratio, $\dot{a}_{current}/\dot{a}_{C\&A}$, between the cavity growth rate from the proposed method, $\dot{a}_{current}$, and that by Chen and Argon (1981), $\dot{a}_{C\&A}$, is 1.71. The result matches only at the initial point ($a/L = 0.1$) and at the final point ($a/L = 0.5$). Since the initial cavity shape is spherical in the fully-coupled method, it matches with the prediction based on the spherical shape assumption by Chen and Argon (1981). The fact that the two predictions match at the final point implies the crack-like cavity shape at $a/L = 0.5$. This result implies that, as opposed to an abrupt change from a sphere to a crack, gradual shape change occurs between these two points. This demonstrates the adverse effect of gradual cavity shape change on the cavity growth rate, and the cavity growth rate based on the assumed cavity shape simply cannot be used in this transition range.

In Fig. 18 ($a_I/L = 0.1$ and $\alpha = 10$), the proposed numerical analysis predicts faster cavity growth rates in the transition range and the gradual transition is again observed. The maximum difference occurs at $a/L = 0.28$, where the proposed result predicts 565 and the result by Chen and Argon (1981) predicts 350. The cavity growth rate ratio, $\dot{a}_{current}/\dot{a}_{C\&A}$, at $a/L = 0.2, 0.25, 0.28, 0.3, 0.35$, and 0.4 is 1.5, 1.6, 1.61, 1.6, 1.4, and

1.3, respectively. The cavity growth rate predicted by the fully-coupled method is larger than the prediction based on the assumed cavity shape (sphere) for $a/L = 0.14 \sim 0.7$. The smaller α value means larger surface diffusion as in Eq. (30). Therefore, the cavity shape tends to remain spherical at least in the initial stage of growth. This is clearly demonstrated in the initial region, $a/L = 0.1 \sim 0.14$, where the prediction by the fully-coupled method matches with the prediction based on the spherical cavity shape assumption. The fact that the two predictions closely match for $a/L = 0.5 \sim 0.7$ implies the crack-like cavity shape in this range. This result again demonstrates the adverse effect of gradual cavity shape change on the cavity growth rate.

In Fig. 19 ($a_I/L = 0.316$ and $\alpha = 5.82$), the cavity growth rate predictions are compared for $a/L = 0.316 \sim 2.5$. In this case, the larger a/L range compared to the previous two cases is considered. The larger a/L value means the smaller effective diffusion length 'L' for the same cavity radius 'a'. As 'L' decreases, the effect of the deformation on the cavity growth becomes more important. The cavity growth rate predicted by the fully-coupled method is faster than that by Chen and Argon (1981) for $a/L = 0.316 \sim 0.79$. This implies the transition from spherical to crack-like occurs in this range. For $a/L = 0.79 \sim 2.5$, the cavity growth rate predicted by the fully-coupled method is completely different from that (Chen and Argon (1981)) based on the assumed cavity shape. The cavity growth rate predicted by the fully-coupled method is slower than that by Chen and Argon (1981) for $a/L = 0.79 \sim 2.22$ and is faster than that by Chen and Argon (1981) for $a/L = 2.22 \sim 2.5$. This implies that the cavity shape does not converge to crack-like shape.

In the cavity growth rate calculation based on the assumed cavity shape (Chen and Argon (1981)), it is assumed that the cavity volume growth rate (\dot{V}_1 and \dot{V}_2) is all related with the atomic flux at cavity tip, ' $j_{s(tip)}$ '. Therefore, Chen and Argon (1981) assumed two types of final cavity shape: spherical cavity shape when the surface diffusion is fast or crack-like cavity shape when the surface diffusion is slow. However, the volume growth

rate \dot{V}_2 , which is the cavity volume growth rate due to deformation, contributes to the elongation of the cavity in the loading direction. Therefore, as a/L increases and the surface diffusion controls the cavity growth, the final cavity shape cannot be simply assumed to be spherical or crack-like. The cavity shape evolution will be further investigated later in this section.

In Fig. 20 ($(a_I/L) = 1.0$ and $\alpha = 1.0$), the cavity growth rate predicted by the fully-coupled method is completely different from that by Chen and Argon (1981) for $a/L = 1.0 \sim 9.0$. In this a/L range, the volume growth rate due to deformation and jacking, \dot{V}_2 , becomes more important compared to the previous three cases. The cavity growth rate predicted by the fully-coupled method is slower than the prediction (Chen and Argon (1981)) based on the assumed cavity shape for the entire a/L range. This implies that the cavity growth rate based on the assumed cavity shape simply cannot be used for this case.

Figure 21~24 show the cavity aspect ratio variation (c/a) versus a/L for the cases shown in Fig. 17~20, where 'c' is the cavity minor radius (as shown in Fig. 7). The aspect ratio variation based on the spherical cavity shape assumption, the crack-like cavity shape assumption, and the sphere and crack-like combined assumption (Chen and Argon (1981)) are included for the comparison purpose. The initial aspect ratio is 0.615 for all cases.

In Fig. 21 ($a_I/L = 0.1$ and $\alpha = 16.2$), the initial aspect ratio predicted by the fully-coupled method is 0.615 and the final aspect ratio is 0.32. The initial aspect ratio based on the crack-like shape assumption is 0.96 and the final aspect ratio is 0.23 while the aspect ratio based on the spherical shape assumption remains 0.615. The aspect ratio change based on the combined cavity shape assumption shows the abrupt change at $a/L = 0.18$. The aspect ratio predicted by the fully-coupled method decreases gradually in the transition range. This demonstrates that the initial spherical shape cavity gradually changes to crack-like cavity. In addition, the gradual decrease of the aspect ratio predicted by the fully-coupled method explains the faster cavity growth

rate compared to the cavity growth rate based on the combined cavity shape assumption as shown in Fig. 17. The final aspect ratio predicted by the fully-coupled method does not match with the aspect ratio based on the crack-like assumption at $a/L = 0.5$ even if the cavity growth rate converges as shown in Fig. 17.

In Fig. 22 ($a_I/L = 0.1$ and $\alpha = 10$), the final aspect ratio predicted by the fully-coupled method is 0.37. The initial aspect ratio based on the crack-like shape assumption is 1.56 and the final aspect ratio is 0.25. The aspect ratio predicted by the fully-coupled method is similar as the initial value for $a/L = 0.1 \sim 0.16$. This demonstrates that the surface diffusion is fast enough to maintain the spherical shape for this range. It explains the reason why the cavity growth rate match for the initial transition range as shown in Fig. 18. The aspect ratio based on the combined cavity shape assumption shows the abrupt change at $a/L = 0.31$. The aspect ratio predicted by the fully-coupled method decrease gradually for $a/L = 0.16 \sim 0.7$. It implies again that the initial spherical shape cavity gradually changes to crack-like cavity for this case. The final aspect ratio predicted by the fully-coupled method, 0.37, is higher than that for the previous case shown in Fig. 21, 0.32, since the lower α value is employed in this case.

In Fig. 23 ($a_I/L = 0.316$ and $\alpha = 5.82$), the final aspect ratio predicted by the fully-coupled method is 0.4. The initial aspect ratio based on the crack-like shape assumption is 1.46 and the final aspect ratio is 0.09. The aspect ratio change based on the assumed cavity shape shows the abrupt change at $a/L=0.8$. The aspect ratio predicted by the fully-coupled method decrease gradually and then saturate to 0.4. The aspect ratio from the fully-coupled analysis does not follow that based on the crack-like shape assumption. This demonstrates that the cavity does not change to crack-like shape. In addition, it explains the difference in the cavity growth rate as shown in Fig. 19.

In Fig. 24 ($(a_I/L) = 1.0$ and $\alpha = 1.0$), the final aspect ratio predicted by the fully-coupled method is 1.24. The initial aspect ratio based on the crack-like shape assumption is 1.61 and the final aspect ratio is 0.047. The aspect ratio change based on

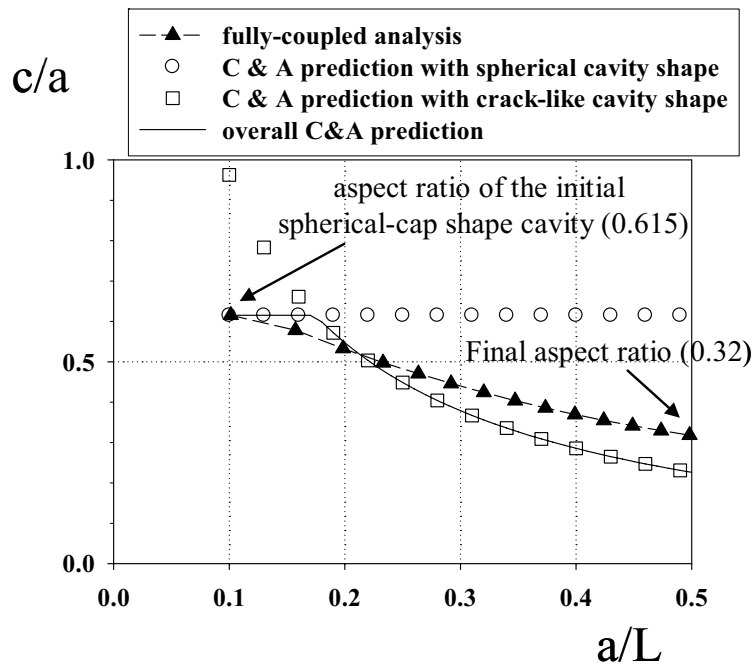


Figure 21: Cavity aspect ratio variation during evolution of spherical-cap shape cavity for $a_1/L = 0.1$ and $\alpha = 16.2$ is shown. The aspect ratio by the fully-coupled method decrease gradually.

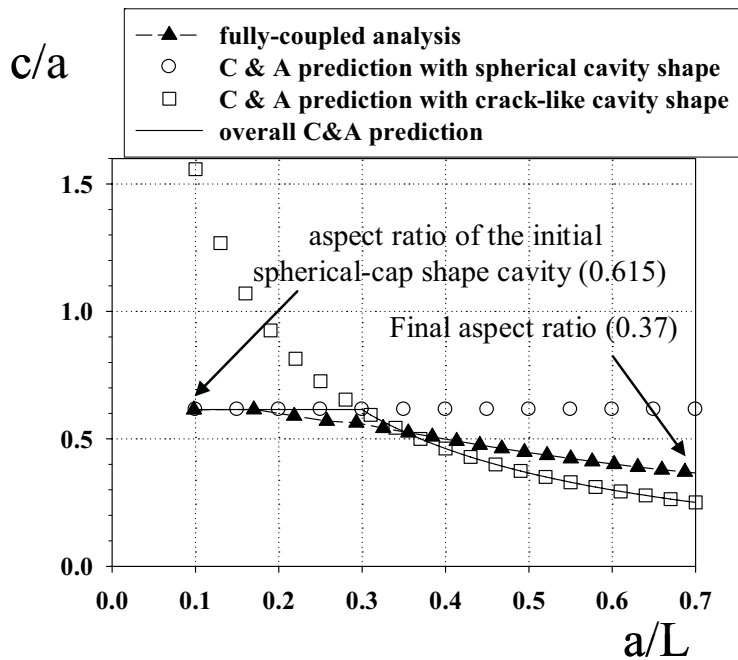


Figure 22: Cavity aspect ratio variation during evolution of spherical-cap shape cavity for $a_1/L = 0.1$ and $\alpha = 10.0$ is shown. Cavity maintains the initial aspect ratio until a/L reaches 0.16, since surface diffusivity is higher compared to the case of Fig. 1.21 (lower α value).

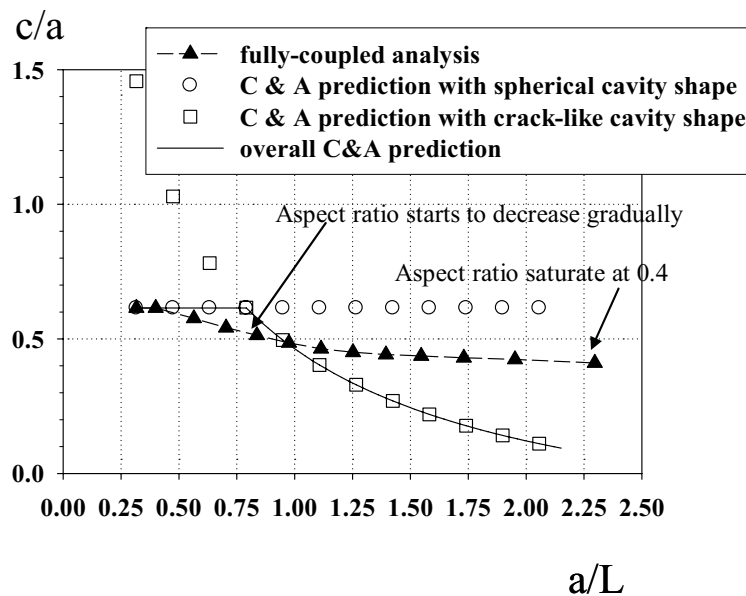


Figure 23: Cavity aspect ratio variation during evolution of spherical-cap shape cavity for $a_l/L = 0.316$ and $\alpha = 5.82$ is shown. The aspect ratio by the fully-coupled method saturates at much higher value ($c/a = 0.4$) than that based on the crack like cavity shape assumption ($c/a = 0.09$).

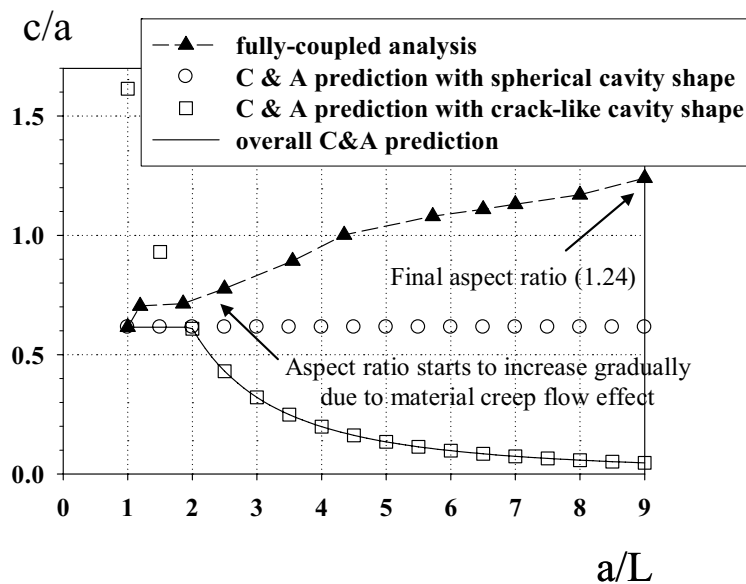


Figure 24: Cavity aspect ratio variation during evolution of spherical-cap shape cavity for $a_l/L = 1$ and $\alpha = 1$ is shown. The cavity aspect ratio by the fully-coupled method does not follow those based on the assumed cavity shape. It clearly shows that the initial spherical-cap shape cavity does not evolve to become crack like cavity.

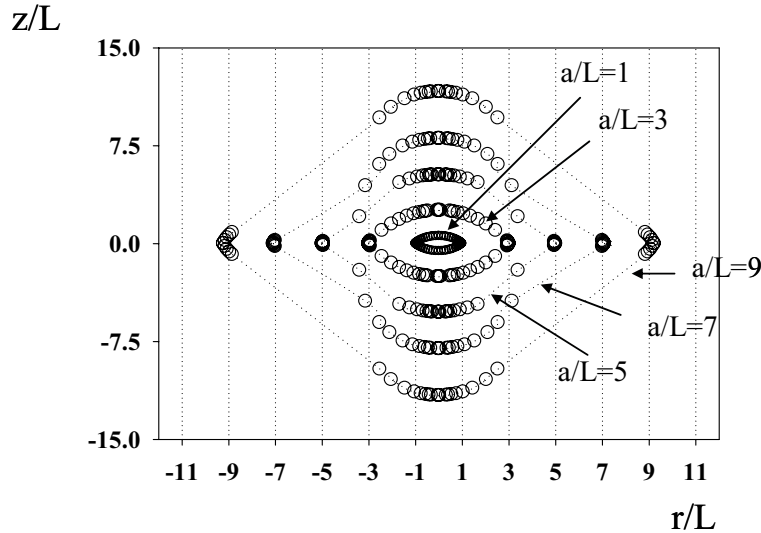


Figure 25: Cavity evolution from spherical-cap shape to V-shape for $a_1/L = 1$, $\alpha = 1$ is shown. Initial spherical-cap shape cavity maintains its original shape until $a/L = 3$. When a/L reaches to 5, cavity shape changes to V-shape, since surface diffusivity is slow and material creep flow effect is significant.

the combined cavity shape assumption shows the abrupt change at $a/L = 2$. The aspect ratio predicted by the fully-coupled method is completely different from that based on the assumed cavity shape. This demonstrates that the cavity shape evolves to the different shape. The cavity shape evolution for this case is further investigated as follows.

Figure 25 shows cavity shapes for the case of $(a_1/L) = 1.0$ and $\alpha = 1.0$ when $a/L = 1, 3, 5, 7$, and 9. The cavity shape is completed by using the axis-symmetric condition. When $a/L = 3$, the initial spherical-shaped cavity maintains its original shape with slightly increased aspect ratio. When $a/L = 5$ and 7, some nodes have negative curvature value because of cavity elongation at the cavity tip in the r -direction due to material diffusion and cavity elongation at the cavity top in z -direction due to the 'jacking' and creep deformation. When $a/L = 9$, cavity shape becomes V-shaped.

3.4 Comparison of numerical cavity growth prediction with experiments

Based on the results from section 3.3, it is demonstrated that the result by the fully-coupled method is physically more reasonable than that based on

the combined cavity shape assumption in regimes where both surface diffusion and deformation enhanced grain boundary diffusion are important. In this section, the fully-coupled method is employed to predict the experimental result by Goods and Nix (1978).

Goods and Nix (1978) used silver in their study of cavity growth and recorded fracture time ' t_f ', and fracture strain ' ϵ_f ', for each constant stress creep test at several temperatures between 200°C and 550°C. These experimental data and test conditions (test temperature, T , and the remote stress, σ_∞) for each test are shown in Table 1, and the physical constants for silver are shown in Table 2. In this study we assumed that the initial cavity radius, ' a_i ', is to be $0.785\mu\text{m}$ and ' a_f ', is to be $1.1\mu\text{m}$, which was first reported in Goods and Nix's [1978] experiment and was later modified due to geometric consideration by other authors (Chen and Argon (1981), Pharr and Nix (1979)).

In order to use the experimental results in verifying the fully-coupled method, the normalized cavity growth rate, $\frac{4\pi h(\psi)}{\epsilon a} \frac{da}{dt}$, versus the normalized cavity radius, a/L , are obtained from the experimental results by Goods and Nix (1978). Following the procedure by Chen and Argon (1981), the normalized cavity growth rate $\frac{4\pi h(\psi)}{\epsilon a} \frac{da}{dt}$ is as-

Table 1: Experimental conditions reported by Goods and Nix (1978) and a/L value

Test no.	T (K)	σ_{∞} (Pa)	t_f (Sec.)	ϵ_f	$\dot{\epsilon} (\cong \epsilon_f/t_f)$ (/Sec.)	L (m)	a/L
1	823	1.38E+06	3.07E+05	0.006	1.95E-08	1.07E-05	0.07
2	823	2.76E+06	5.58E+04	0.008	1.34E-07	7.10E-06	0.11
3	823	3.45E+06	2.52E+04	0.006	2.50E-07	6.22E-06	0.13
4	823	4.83E+06	1.10E+04	0.006	5.82E-07	5.25E-06	0.15
5	823	6.89E+06	2.20E+03	0.006	2.91E-06	3.46E-06	0.23
6	823	8.69E+06	1.29E+03	0.009	6.59E-06	2.85E-06	0.28
7	823	1.09E+07	3.20E+02	0.010	3.09E-05	1.83E-06	0.43
8	823	1.38E+07	1.35E+02	0.019	1.44E-04	1.19E-06	0.66
9	673	6.89E+06	7.70E+04	0.006	8.18E-08	4.58E-06	0.17
10	673	9.74E+06	1.75E+04	0.012	6.57E-07	2.56E-06	0.31
11	673	1.38E+07	4.99E+03	0.020	4.07E-06	1.57E-06	0.50
12	673	2.07E+07	9.24E+02	0.022	2.42E-05	9.90E-07	0.79
13	673	2.76E+07	3.90E+02	0.033	8.51E-05	7.17E-07	1.09
14	673	3.45E+07	1.80E+02	0.025	1.36E-04	6.61E-07	1.19
15	673	4.48E+07	5.62E+01	0.027	4.82E-04	4.73E-07	1.66
16	573	1.09E+07	3.42E+05	0.012	3.36E-08	2.97E-06	0.26
17	573	1.72E+07	2.70E+04	0.016	6.07E-07	1.32E-06	0.60
18	573	2.76E+07	4.50E+03	0.017	3.87E-06	8.32E-07	0.94
19	573	3.45E+07	2.14E+03	0.024	1.12E-05	6.28E-07	1.25
20	573	4.48E+07	6.00E+02	0.033	5.45E-05	4.05E-07	1.94
21	573	5.52E+07	8.10E+02	0.030	3.70E-05	4.94E-07	1.59
22	573	6.89E+07	3.15E+02	0.025	7.94E-05	4.12E-07	1.90
23	573	8.68E+07	1.85E+01	0.007	3.89E-04	2.62E-07	3.00
24	473	2.17E+07	3.96E+05	0.013	3.18E-08	1.07E-06	0.73
25	473	3.45E+07	5.04E+04	0.032	6.29E-07	4.62E-07	1.70
26	473	4.83E+07	1.76E+04	0.028	1.59E-06	3.79E-07	2.07
27	473	6.89E+07	3.31E+03	0.014	4.23E-06	3.08E-07	2.55

Table 2: Material properties of silver

γ_s	ψ	D_{gbo}	δ_{gb}	Q_{gb}	Ω	D_{so}	δ_s	Q_s
J/m ²	Deg.	m ² /sec	m	J/mole	m ³	m ² /sec	m	J/mole
1.14*	70*	1.2E-5*	5E-10*	90016.2*	1.71E-29*	2.5E-06 ¹ 4.5E-06 ² 1.4E-06 ³	2.57E-10*	84500 ¹ 49100 ² 67400 ³

* Goods, S. H.; Nix, W. D. (1978): *Acta metall*, 26, 739,

Chuang, T. Z. et al. (1979): *Acta metall*, 27, 265,

Robinson, J. T.; Peterson, N. J. (1972): *Surf. Sci.*, 31, 586,

Turnbull, D. (1951): *J. appl. Phys.*, 22, 634

¹ Goods, S. H.; Nix, W. D. (1978): *Acta metall*, 26, 739

² Chuang, T. Z. et al. (1979): *Acta metall*, 27, 265

³ Gjostein, N. A. (1974): Diffusion Seminar, ASM, Cleveland

sumed to be constant due to short testing time and can be approximated (Chen and Argon (1981)) by

$$\frac{4\pi h(\psi)}{\dot{\epsilon}a} \frac{da}{dt} \cong \frac{4\pi h(\psi)}{\epsilon_f} \ln \frac{a_f}{a_I}, \quad (30)$$

where ψ is assumed to be 70 degree (Table 2). In calculating L from Eq. (25) and Eq. (4), creep strain rate is approximated by $\frac{\epsilon_f}{t_f}$ and the material properties of silver, such as D_{gbo} , δ_{gb} , Q_{gb} , and Ω in Table 2, are used. The a/L value is approximated by a_I/L and values for each test are shown in Table 1.

In order to employ the fully-coupled method in predicting the experimental result, it is necessary to calculate two parameters: diffusivity ratio, α (Eq. (29)), and the ratio between the initial sintering stress and the remote stress, $(\sigma_o)_I/\sigma_\infty$. The initial sintering stress, $(\sigma_o)_I$, is obtained using the following relation,

$$\begin{aligned} \sigma_o &= \gamma_s(\kappa_1 + \kappa_2) = \gamma_s(\sin \psi/a_I + \sin \psi/a_I) \\ &= 2\gamma_s \sin \psi/a_I \quad (31) \end{aligned}$$

where the relation shown in Eq. (6) and the initial spherical cavity shape assumption are used. The values of these two parameters, α and $(\sigma_o)_I/\sigma_\infty$, depend on test condition. In calculating these parameters, physical constants for silver are required. As shown in Table 2, different values for surface diffusion constants for silver, including the values from Goods and Nix experiment (1978), are reported. Goods and Nix (1978) calculated the surface pre-exponent value, D_{so} , and the surface activation energy, Q_s , from the rupture time vs. stress plot and the reciprocal of the time to rupture vs. the reciprocal of the test temperature plot, respectively. In order to obtain these plots, they (Goods and Nix (1978)) used the constant stress creep test results. Therefore physical constants reported by Goods and Nix (1978) are used in this study.

D_s and D_{gb} are obtained from Eq. (4) and Table 2. The diffusivity ratio, D_s/D_{gb} is used in obtaining the α value as in Eq. (30). These values for each test are listed in Table 3. As shown in Table 3, the largest α value is 24 and the smallest α value is 16.2. $(\sigma_o)_I/\sigma_\infty$ should be less than 1 under a

cavity growth condition. These values for test 1 or 2 are larger than 1 or very close to 1, which implies no cavity growth. Therefore they are omitted from further analysis. This leads to the largest $(\sigma_o)_I/\sigma_\infty$ value, 0.8, and the smallest $(\sigma_o)_I/\sigma_\infty$ value, 0. In applying the fully-coupled method to this experimental condition, initial spherical cavity is assumed to have one of the following two conditions: $a_I/L = 0.1$, $\alpha = 16.2$, $(\sigma_o)_I/\sigma_\infty = 0.0$ and $a_I/L = 0.12$, $\alpha = 24$, $(\sigma_o)_I/\sigma_\infty = 0.8$. The reason for choosing the specific a_I/L , α , and $(\sigma_o)_I/\sigma_\infty$ values for the two conditions is as follows.

The a_I/L value is assumed to be around 0.1 since the smallest a_I/L value reported in Table 1 is 0.13. According to the reported results by Needleman and Rice (1980) and the current study, an increase of the $(\sigma_o)_I/\sigma_\infty$ value significantly decreases the cavity growth rate. Therefore, the cavity growth rate with $(\sigma_o)_I/\sigma_\infty = 0.0$ is the fastest and the cavity growth rate with $(\sigma_o)_I/\sigma_\infty = 0.8$ is the slowest for a given constant α value. Compared to the effect of the stress ratio, $(\sigma_o)_I/\sigma_\infty$, on the cavity growth rate, the effect of α value on the cavity growth rate is not significant. Therefore, any combination of α and $(\sigma_o)_I/\sigma_\infty$ from $\alpha = 16.2 \sim 24$, and $(\sigma_o)_I/\sigma_\infty = 0.0$ represent the upper bound (fast normalized cavity growth rate) and any combination of α and $(\sigma_o)_I/\sigma_\infty$ from $\alpha = 16.2 \sim 24$, and $(\sigma_o)_I/\sigma_\infty = 0.8$ represent the lower bound (slow normalized cavity growth). In this study, the condition, $a_I/L = 0.1$, $\alpha = 16.2$, and $(\sigma_o)_I/\sigma_\infty = 0.0$, is chosen to represent the upper bound and the condition, $a_I/L = 0.12$, $\alpha = 24$, and $(\sigma_o)_I/\sigma_\infty = 0.8$, is chosen to represent the lower bound. This condition represents the narrowest bound of any possible combination of α and $(\sigma_o)_I/\sigma_\infty$.

Figure 26 shows the normalized cavity growth rate versus the normalized cavity radius for Goods and Nix (1978) experiment, the prediction from the fully-coupled method, and the prediction based on the spherical cavity shape assumption with $(\sigma_o)_I/\sigma_\infty = 0.0$ and 0.8. As shown in Fig. (26), some of the experimental data points (denoted by \bullet) are bounded by the prediction based on spherical cavity shape assumption with

Table 3: α and the stress ratio between the initial sintering stress and the remote stress

Test no.	Temp (K)	D_s/D_{gb}	α	$(\sigma_o)_I/\sigma_\infty$
1	823	2.40E-01	1.62E+01	1.98E+00
2	823	2.40E-01	1.87E+01	9.89E-01
3	823	2.40E-01	1.95E+01	7.91E-01
4	823	2.40E-01	2.12E+01	5.65E-01
5	823	2.40E-01	2.06E+01	3.96E-01
6	823	2.40E-01	2.10E+01	3.14E-01
7	823	2.40E-01	1.89E+01	2.50E-01
8	823	2.40E-01	1.71E+01	1.98E-01
9	673	2.35E-01	2.39E+01	3.96E-01
10	673	2.35E-01	2.13E+01	2.80E-01
11	673	2.35E-01	1.98E+01	1.98E-01
12	673	2.35E-01	1.93E+01	1.32E-01
13	673	2.35E-01	1.90E+01	9.90E-02
14	673	2.35E-01	2.03E+01	7.92E-02
15	673	2.35E-01	1.96E+01	6.09E-02
16	573	2.38E-01	2.41E+01	2.50E-01
17	573	2.38E-01	2.02E+01	1.58E-01
18	573	2.38E-01	2.03E+01	9.90E-02
19	573	2.38E-01	1.97E+01	7.92E-02
20	573	2.38E-01	1.81E+01	6.09E-02
21	573	2.38E-01	2.21E+01	4.95E-02
22	573	2.38E-01	2.26E+01	3.96E-02
23	573	2.38E-01	2.02E+01	3.14E-02
24	473	2.51E-01	1.99E+01	1.26E-01
25	473	2.51E-01	1.65E+01	7.92E-02
26	473	2.51E-01	1.77E+01	5.65E-02
27	473	2.51E-01	1.90E+01	3.96E-02

$(\sigma_o)_I/\sigma_\infty = 0.0$ and 0.8 . However, some of the experimental data points (denoted by \blacktriangle) are not bounded by the prediction based on the spherical cavity shape assumption. This implies that some of initial cavities considered in Goods and Nix (1978) are already crack-like at the start of the analysis and the cavity shape evolution from the spherical to the crack-like needs to be considered in predicting the experimental data points. As shown in Fig. 26, all the experimental data points excluding test 1 and test 2 are bounded by the fully-coupled method prediction for the two extreme cases. This demonstrates validity of the fully-coupled method developed in this work.

In this study, the one-to-one match between the experimental result and prediction by the fully-

coupled method is not possible, since the initial cavity shape is not known and precise value of the initial and final cavity radius is not reported for each test. If these information are available, individual test data can be predicted based on the fully coupled method.

Chen and Argon (1981) successfully predicted the experimental results by Goods and Nix (1978) using the cavity growth rate prediction based on the combined cavity shape assumption. However, specific values of surface diffusion material properties employed for the analysis (Chen and Argon (1981)) are not mentioned in their work and it is not clear how two extreme values of α , 13 and 4, are chosen. In this study, the α and $(\sigma_o)_I/\sigma_\infty$ values are based on the material data obtained by

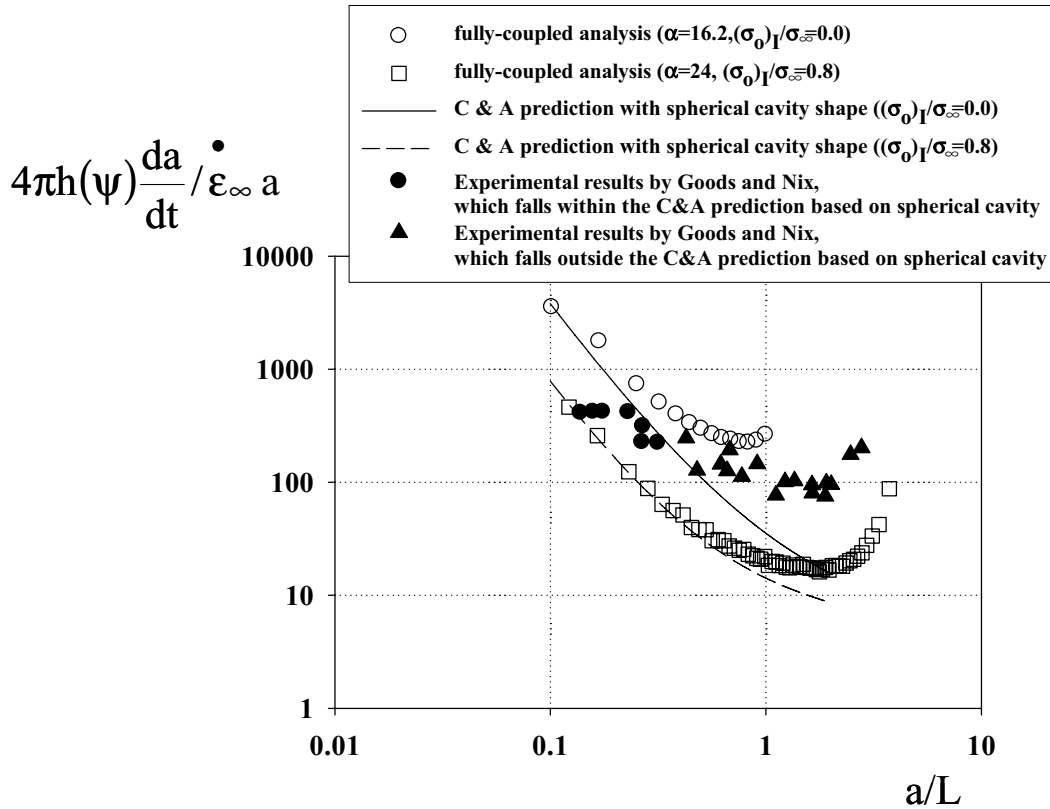


Figure 26: Normalized cavity growth rate vs. normalized cavity radius are shown. The experimental results are bounded by the cavity growth rates predicted by the fully coupled method ($a_1/L = 0.1$, $\alpha = 16.2$, $\sigma_o/\sigma_\infty = 0$ (hollow circle) and $a_1/L = 0.12$, $\alpha = 24$, $\sigma_o/\sigma_\infty = 0.8$ (hollow square)). Since different material constants for surface diffusion are reported and the simple assumptions are employed on obtaining the data points for the experimental results, the direct comparison between the each experimental data points and the numerical simulation results is not possible. However, from the distribution of each data points in this figure, it is clear that the cavity evolves from the spherical-cap shape to other shape in this range of a/L and α values.

Goods and Nix (1978), and they are more carefully chosen compared to those by Chen and Argon (1981). In addition, Chen and Argon (1981) assumed that the sintering stress is zero. In this study, no such assumption is employed in obtaining the results.

4 Discussion

Arai et al. (1996) reported cavity shape evolution from the spherical-shape to the V-shape under load controlled cyclic test conditions. Since the fully-coupled method developed in this work is developed for the cases of constant loading, the quantitative comparison between the experimental result (Arai et al. (1996)) and the prediction

based on the fully-coupled method is not readily available. However, it is possible to make a qualitative comparison.

They (Arai et al. (1996)) argued that the sharp creep strain rate increases upon stress reversal or accumulated plastic strain can be possible reasons for this cavity shape evolution. According to our recent numerical study (Oh et al. (2007)) on the constrained cavity growth, it was shown that, under load controlled cyclic test conditions, the grain material experiences sharp creep strain rate increases at stress reversals, which increases creep flow effects on the cavity growth. In this study, it was shown that the initial spherical cavity evolves to the V-shaped cavity when the creep

strain rate increases ($a/L > 1.0$). While the cyclic loading condition used in the experiments was not simulated, the cavity shape change from a sphere to a V-shape qualitatively matches the experimental observation. This qualitative match can be attributed to the fully coupled nature of our developed method combining the surface diffusion and the deformation enhanced grain boundary diffusion.

The material viscoplastic deformation, which causes cavity shape change, “jacking” at the cavity tip, and the decrease of the effective diffusion length along the grain boundary, have never been fully coupled with the surface/grain boundary diffusion in the cavity growth study. In this work, possible cavity shape evolution from the spherical to the V-shaped is numerically predicted for the first time and the adverse effect of gradual cavity shape change on the cavity growth rate is demonstrated.

In order to achieve the quantitative agreement between the prediction from the fully-coupled method and the experimental result (Arai et al. (1996)), the following features need to be considered in the future. In this study, numerical simulations under uniaxial tensile loading condition were studied. According to our recent numerical study (Oh et al., will appear on *J. of Eng. Mat. Tech.*) on the grain boundary cavitation, it was shown that under uniaxial tensile loading conditions, the multiaxial stress state develops around the cavities on the cavitating grain boundary. The effect of the multiaxial stress on the cavity growth rate is numerically studied by Sham and Needleman (Sham and Needleman (1982), Sham and Needleman (1983)). They reported that cavity growth rate depends on the stress ratio between the Mises type effective stress and the hydrostatic stress state based on the assumption of fast surface diffusion. In order to accurately predict the cavity growth rate under multiaxial stress condition, the fully coupled method proposed in this study needs to be expanded to include the multiaxial stress state in the boundary condition.

In this study, a steady state creep flow rule is employed to represent the material inelastic constitutive relation. The steady state creep flow

rule, which is implemented in the proposed fully-coupled method, is accurate enough when a constant loading is applied or cavity is nucleated when the strain hardening of the grain material is saturated. However, in all practical loading conditions, a cyclic loading condition is more realistic than a constant loading condition. The recent numerical study (Oh et al., will appear on *J. of Eng. Mat. Tech.*) on the grain boundary cavitation shows that strain hardening type creep flow rule is more accurate than the steady state creep flow rule in representing the material inelastic constitutive relation under cyclic loading condition. Under this condition, it is necessary to employ the strain hardening type creep flow rule in the fully-coupled method.

5 Conclusion

In this study, a unified numerical method is proposed, where the surface and grain boundary diffusion and material viscoplastic deformation are considered. The proposed unified method is verified by comparing the obtained results for extreme cases with the previous works (Needleman and Rice (1980), Martinez and Nix (1982)).

In the first extreme case, the loading condition and the material constants are chosen so that the deformation is not important and matter diffusion is the dominant cavity growth mechanism. When the surface diffusion controls the overall diffusion process, it is shown that the cavity shape changes from spherical-cap shape to crack-like shape as shown by Martinez and Nix (1982). In addition, it is shown that the cavity coalescence time matches with the previous works (Chuang et al. (1979), Martinez and Nix (1982)).

In the second extreme case, the loading condition and the material constants are chosen so that matter diffusion is enhanced by the material viscoplastic deformation. When the grain boundary diffusion controls the overall diffusion process, the cavity is shown to maintain initial spherical shape as it grows. As opposed to the work by Needleman and Rice (1980), the continuous cavity growth is numerically predicted based on the given initial cavity geometry. Therefore, this result confirms the previous work (Needleman and

Rice (1980)) where the spherical cavity is assumed to maintain its spherical shape as it grows under the fast surface diffusion. In the previous numerical work (Needleman and Rice (1980)), the cavity growth rate is discretely calculated for chosen cavity radius. The cavity volume growth rates are calculated at the same cavity radius as in Needleman and Rice (1980). It is shown that one to one match between our results and the previous results (Needleman and Rice (1980)) is achieved. This quantitative verification demonstrates the validity of our approach.

Upon verification of the proposed method by considering extreme cases, a fully coupled case of the surface diffusion controlled cavity growth in the deformation enhanced diffusion region is examined. When the diffusion is more important than the phenomena called “jacking” (upward movement of cavity surface) and material viscoplastic deformation, the transitional shape change from the initial spherical-cap shaped cavity to the crack-like cavity is predicted. The cavity growth rate in this transition range is found to be much faster than that obtained by combining the cavity growth rates with two extreme cavity shape (Chen and Argon (1981)) (spherical and crack-like). This demonstrates that the transitional cavity shape change, which has never been examined in the previous work, significantly accelerates the cavity growth rates. Therefore, a fully coupled model needs to be employed for accurate life prediction.

When the “jacking” and material viscoplastic deformation is more important than diffusion, the transitional shape change from the initial spherical cavity to the V-shaped cavity is predicted. While V-shaped cavity has never been predicted in the previous work, Arai et al. (1996) experimentally observed the V-shaped cavity under cyclic loading condition. Unfortunately, quantitative comparison between the experimental results and the proposed method could not be made due to unknown material parameters and different loading condition. However, the proposed fully coupled approach provides the research community a possible mechanism of experimentally observed transitional cavity shape change from a

spherical cavity to V-shaped cavity.

Upon obtaining physically reasonable result for a fully coupled case of the surface diffusion controlled cavity growth in the deformation enhanced diffusion region, the fully-coupled method is employed to predict the experimental result (Goods and Nix (1978)). The one-to-one match between the experimental result and prediction based on the developed method is not possible due to lack of parameters such as initial cavity shape and dimension. However, it is shown that all the cavity growth rates reported in the experiment are bounded by the fully-coupled method prediction for the two extreme cases. This demonstrates the validity of the fully-coupled method in regimes where both surface diffusion and deformation enhanced grain boundary diffusion are important. .

As a future work, it is desirable to include features, such as the multi-axial stress state and the strain hardening type creep flow rule, in the fully coupled method so that it can be readily applied to life prediction under cyclic loading condition. In addition, recent implicit algorithms by Akamatsu, Nakane, and Ohno (2005) illustrate efficient techniques for solving visco-plastic and creep problems along with including phase transformation plasticity effects. The implementation of these concepts will likely reduce solution times for the problems considered here and will be considered in future work as well.

References

- Akamatsu, M.; Nakane, K.; Ohno, N.** (2005): An Implicit Integration Scheme for a Nonisothermal Viscoplastic, Nonlinear Kinematic Hardening Model, *CMES: Computer Modeling in Engineering & Sciences*, 10(3), 217-228.
- Arai, M.; Ogata, T.; Nitta** (1996): *JSME Int. Journal A*, 39(3), 382.
- Beere, W.; Speight, M. V.** (1978): *Metal Sci.*, 4, 172.
- Chen, I.-W.; Argon, A. S.** (1981): *Acta Metallurgica*, 29, 1759.
- Chuang, T.-J.; Rice, T. R.** (1973): *Acta Metallurgica*, 21, 1625.

- Chuang, T.-J.; Kagawa, K. I.; Rice, J. R.; Sills, L. B.** (1979): *Acta Metall. Mater.*, 27, 265.
- Cocks, A. C. F.; Pan, J.** (1993): *Int. J. of Fracture*, 60, 249.
- Edward, G. H.; Ashby, M. F.** (1979): *Acta Metall.*, 27, 1505.
- Goods, S. H.; Nix, W. D.** (1978): *Acta Metallurgica*, 26, 739.
- Hull, D.; Rimmer, D. E.** (1959): *Phil. Mag.*, 4, 673.
- Martinez, L.; Nix, W. D.** (1981): *Metall. Trans. A*, 12A, 23.
- Needleman, A.; Rice, J. R.** (1980): *Acta Metallurgica* 28, 1315.
- Oh, J.; Brust, F. W.; Katsube, N.** (2007): *J. Eng Mat. Tech.*, 129, 1-10.
- Pan, J.; Cocks, A. C. F.** (1993a): *Int. J. of Fracture* 60, 121.
- Pan, J.; Cocks, A. C. F.** (1993b): *Computational Materials Science*, 1, 95.
- Pan, J.; Cocks, A. C. F.** (1995): *Acta Metall. Mater.*, 43(4), 1395.
- Pharr, G. M.; Nix, W. D.** (1979): *Acta Metallurgica*, 27, 1615.
- Raj, R.** (1975): *Metallurgical Transactions A*, 6A, 1499.
- Raj, R.** (1978): *Acta Metallurgica*, 26, 341.
- Rice, J. R.** (1979): Time Dependent Fracture of Materials at Elevated Temperature (edited by S. Wolf), p. 130, U.S. Department of Energy Report CONF 790236 UC-25, Germantown, Md.
- Sham, T.-L.; Needleman, A.** (1982): Effects of Triaxial Stressing on Creep Cavitation of Grain Boundaries. Division of Engineering, Brown University.
- Sham, T.-L.; Needleman, A.** (1983): *Acta Metall.*, 31(6), 919.
- Speight, M. V.; Harris, J. E.** (1967): *Metal. Sci. J.*, 1, 83.
- Sun, B.; Suo, Z.; Cocks, A. C. F.** (1996): *J. Mech. Phys.*, 44(4), 559.
- Suo, Z.; Wang, W.** (1994): *J. Appl. Phys.*, 76(6), 15.
- Vitek, V.** (1978): *Acta Metall.*, 26.
- Weertman, J.** (1973): *Scripta Metall.*, 7, 1129.
- Yuan, X. G. and Zhang, R. J.** (2006): Nonlinear Dynamical Analysis in Incompressible Transversely Isotropic Nonlinearly Elastic Materials: Cavity Formation and Motion in Solid Spheres, *CMC: Computers, Materials, and Continua*, Vol. 3(3), 119-130.

